Ain Shams Engineering Journal (2012) 3, 79–103

Ain Shams University

Ain Shams Engineering Journal

www.elsevier.com/locate/asej
www.sciencedirect.com

CIVIL ENGINEERING

# Parametric analysis of tunnel behavior in jointed rock

H. Madkour *

*Faculty of Engineering, Civil Engineering Dept., South Valley University, Egypt*

Received 20 December 2010; revised 3 January 2012; accepted 8 January 2012
Available online 23 February 2012

**KEYWORDS**

Parametric analysis;
Tunneling;
Elastoplastic modeling;
Effective stress;
Jointed rock

**Abstract** Jointed rock masses are often encountered during underground excavation. Many failures of underground openings, during excavation and in operation, are reported closely related to joints.

This paper investigates the impact of three basic factors affecting the tunnel behavior in jointed rock; rock joints density, joints orientation and tunnel depth, respectively. A parametric study has been also conducted using two elastoplastic numerical models; the four-parameters Ottosen plasticity model and Mohr–Coulomb criterion, for concrete lining and rock mass, respectively. Eleven tunnel cases have been analyzed with different combinations of tunnel depth, joint orientation and joint density. The tunnel behavior has been evaluated by investigating; the resulted deformations, evolution of plastic regions and induced stresses in the concrete lining and the surrounding jointed rock.

The obtained numerical results have been analyzed and discussed displaying the importance to consider these factors affecting the behavior of tunnels constructed in jointed rock.



## 1. Background

Many tunneling projects are now underway around the world, including subway tunnels, railway tunnels, rapid railway tunnels, roadway tunnels, electricity tunnels and telecommunication tunnels, etc. The behavior of tunnels is mostly empirical. Generally, the typical support design pattern is adopted based on the rock/soil types, or based on RMR (Rock Mass Rating) values. However, both stress and structure induced failures should be considered in the design of rock support for tunnel design especially in jointed rock [1].

Jointed rock masses are often encountered during underground excavation. Jointed rock exhibits complex mechanical behavior; such as anisotropy, hysteresis, dilatancy, irreversible strain and strongly path-dependent stress-strain relationships which is generally associated with the existence of a great deal of joints (cracks) and their propagation. Joints usually occur in sets which are more or less parallel and regularly spaced. Under some conditions, the joints may lead to big disasters for tunnel construction [2]. Many reported failures of

* Tel.: +20 1005724689; fax: +20 974660789.
E-mail address: h_madkour@yahoo.com



Peer review under responsibility of Ain Shams University.
doi:10.1016/j.asej.2012.01.002

Production and hosting by Elsevier

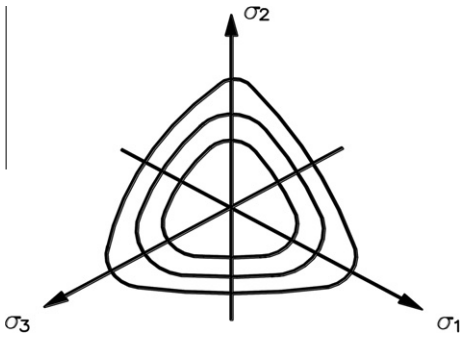


**Figure 1** Initial and failure surfaces for Ottosen criterion [10].

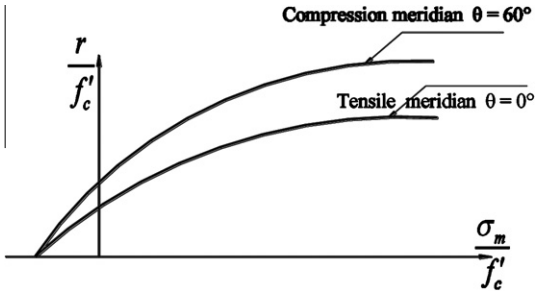


**Figure 2** Shape of meridians for Ottosen [10].

underground openings during excavation and in operation are closely related to joints [3].

Some underground structures have to pass through large-scale jointed rock masses which make underground structures difficult to design and construct. The joints and crannies of jointed rock masses are the cause for rock masses to be discontinuous and hard to be described by a precise mechanical model [4].

The stability of the tunnel is mainly affected by the attributes of the joints, namely, their orientations relative to the tunnel, their spacing, and their shear strengths. Therefore, in this paper a parametric study has been carried out to investigate the effects of tunnel depth, joint spacing and friction angle on tunnel stability [5]. A large number of experiments for intact and jointed rock masses can be found in the literature [4–7]. Such experiments were explained based on Hoek–Brown

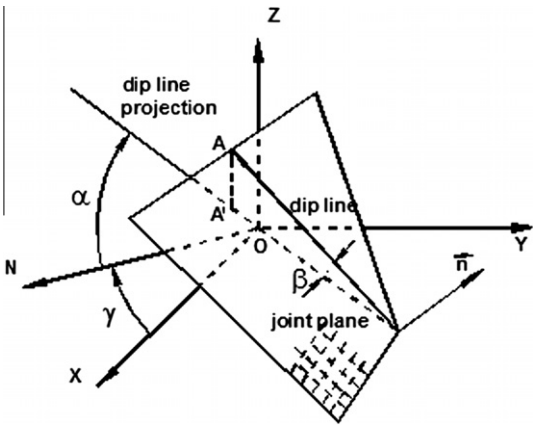


**Figure 4** Orientation system for cracking system for rock mass [15].

failure criteria [6]. However, it has been proved later [4] that this criterion does not apply to materials that exhibit significant anisotropy in strength and deformability (e.g. if the rock mass contains a single dominant joint direction). Kwangho and Yeonjun [7] have shown that unrealistic results were obtained when shotcrete was modeled by the elastic beam element which never fails in numerical calculations. Finally, the two dimensional numerical analysis, have displayed, a more reasonable safety factor of a tunnel is obtained if the continuum (elasto-plastic) element is adopted for the simulation of shotcrete especially under poor ground conditions.

## 2. Scope and objective

The current elastoplastic investigation evaluates the complex tunnel behavior with considering the rock joints as a deterioration state. This consideration of the joints (damage) within the numerical analysis necessitates combined formulation of the plastic flow and damage mechanics. But this combined formulation is a complicated process, due to the interaction of two different dissipative mechanisms.

Since deterioration will lead to a reduction of the loading carrying area with inducing stress concentration around the defects, consequently it may cause a reduction of the yield surface. It has been proved that the failure state depends upon

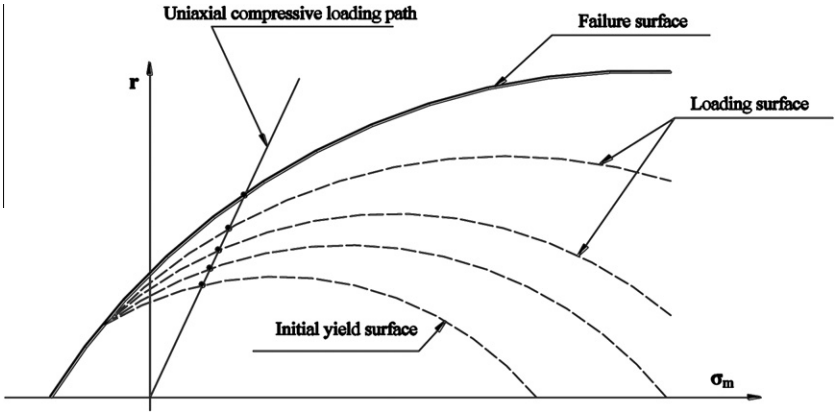


**Figure 3** A non-uniform hardening plasticity model [13].

**Table 1** Model parameters used for rock and concrete.

| | Type | Value |
|---|---|---|
| Rock | $E$ (kN/m$^2$) | $15.0 \times 10^6$ |
| | $v$ | 0.30 |
| | $\gamma$ (kN/m$^3$) | 25.0 |
| | $C$ (kN/m$^2$) | 1100.0 |
| | $\phi$ (°) | 40 |
| Concrete | $E$ (kN/m$^2$) | $35.0 \times 10^6$ |
| | $v$ | 0.2 |
| | $F_c$ (kN/m$^2$) | $35 \times 10^3$ |

**Table 2** The proposed numerical test program and parameters.

| Group | Case no. | Joint density ($\omega$) | Tunnel depth (m) | Dip angle ($\alpha$°) |
|---|---|---|---|---|
| Ref. case | RT | 0.1 | 400 | 90 |
| A | T1 | 0.0 | 400 | – |
| | T2 | 0.2 | 400 | 90 |
| | T3 | 0.4 | 400 | 90 |
| B | T1 | 0.1 | 200 | 90 |
| | T2 | 0.1 | 300 | 90 |
| | T3 | 0.1 | 500 | 90 |
| | T4 | 0.1 | 600 | 90 |
| | T5 | 0.1 | 800 | 90 |
| C | T1 | 0.1 | 400 | 0 |
| | T2 | 0.1 | 400 | 45 |

the actual stress during plastic failure process [8]. However, the yield surface is changing within the continuity of plastic flow. This change should be considered to be dependent upon both the plastic flow and on the deterioration state of the materials.

Accordingly, it appears reasonable to state that "plastic flow occurs only in the undamaged material micro-bonds by means of effective quantities". Therefore, the characterization of the plastic response and the yield function should be formulated in effective stress space [9].

The main objective of this research work is to display and highlight the significant influence of different factors which affect the behavior of a tunnel excavated in jointed rock mass. These factors are; the tunnel depth, and joints configurations (density and orientation). The numerical investigation has been carried out using two elastoplastic numerical models; the four-parameters Ottosen plasticity model and Mohr–Coulomb criterion, for concrete lining and rock mass, respectively.

## 3. Numerical modeling

In this paper, the proposed parametric analysis has been carried out by two elastoplastic numerical models. These models are; the four-parameter Ottosen plasticity [10] and Mohr–Coulomb criteria for concrete lining and rock mass, respectively. For concrete lining, Ottosen criterion has been chosen by the model code 1990 of the CEB-FIP [11].

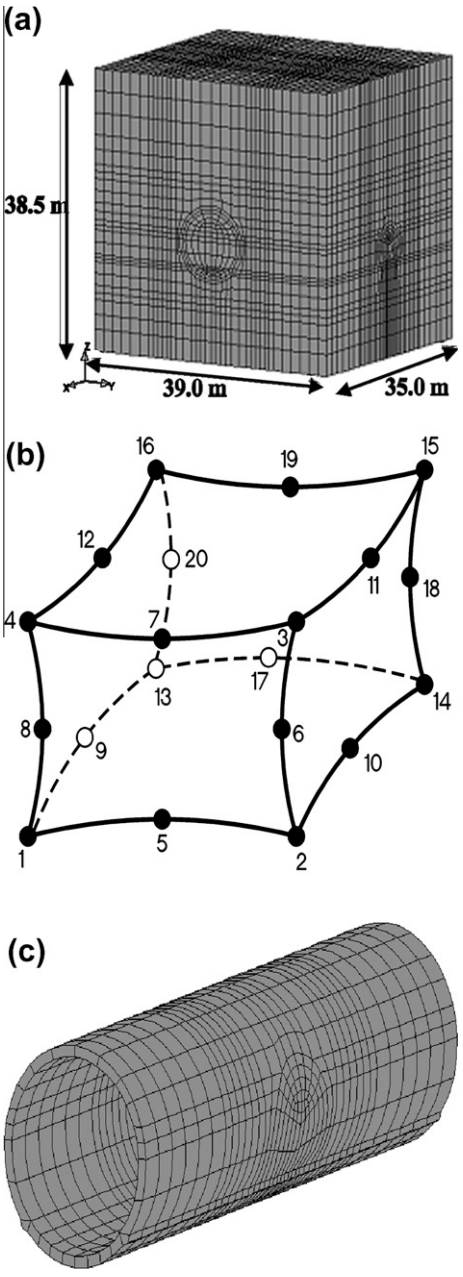


**Figure 5** The layout of Brenner-Base tunnel profile. (a) Rock mass, (b) 20-nodes element, (c) concrete lining.

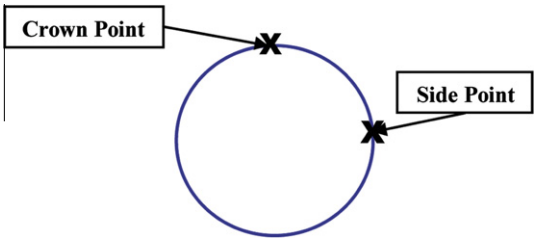


**Figure 6** Investigated critical points on the concrete lining.

The numerical analysis for concrete lining has been carried out using a three-dimensional formulation [10] for Ottosen

**Table 3** Numerical test results.

| Group | Model no. | Concrete lining | | | | | | |
|---|---|---|---|---|---|---|---|---|
| | | *Z*-deformations (mm) | | *Y*-deformations (mm) | *Z*-stresses (kN/m$^2$) | | *Y*-stresses (kN/m$^2$) | |
| | | Crown | Side | Side | Crown | Side | Crown | Side |
| Ref. | RT | 2.5 | 0.6 | 1.5 | −5.0 E3 | −25.0 E3 | −17.0 E3 | −1.5 E3 |
| A | T1 | 2.4 | 0.55 | 1.35 | −5.0 E3 | −.0 E3 | −14.0 E3 | −1.4 E3 |
| | T2 | 2.9 | 0.75 | 1.55 | −5.0 E3 | −25.0 E3 | −17.0 E3 | −1.6 E3 |
| | T3 | 3.3 | 0.9 | 1.6 | −5.0 E3 | −25.0 E3 | −18.0 E3 | −1.7 E3 |
| B | T1 | 0.8 | 0.2 | 0.4 | −1.0 E3 | −8.30 E3 | −5.5 E3 | −0.5 E3 |
| | T2 | 1.5 | 0.4 | 0.8 | −2.5 E3 | −14.0 E3 | −11.0 E3 | 1.0 E3 |
| | T3 | 3.5 | 0.9 | 1.7 | −5.0 E3 | −30.0 E3 | −22.0 E3 | −2.0 E3 |
| | T4 | 4.7 | 1.2 | 2.3 | −6.5 E3 | −40.0 E3 | −28.0 E3 | −2.5 E3 |
| | T5 | 7.7 | 1.5 | 3.1 | −7.0 E3 | −47.0 E3 | −38.0 E3 | −3.5 E3 |
| C | T1 | 2.4 | 0.4 | 1.3 | −3.0 E3 | −23.0 E3 | −15.0 E3 | −1.4 E3 |
| | T2 | 2.3 | 0.5 | 1.4 | −4.0 E3 | −24.0 E3 | −16.0 E3 | −1.4 E3 |

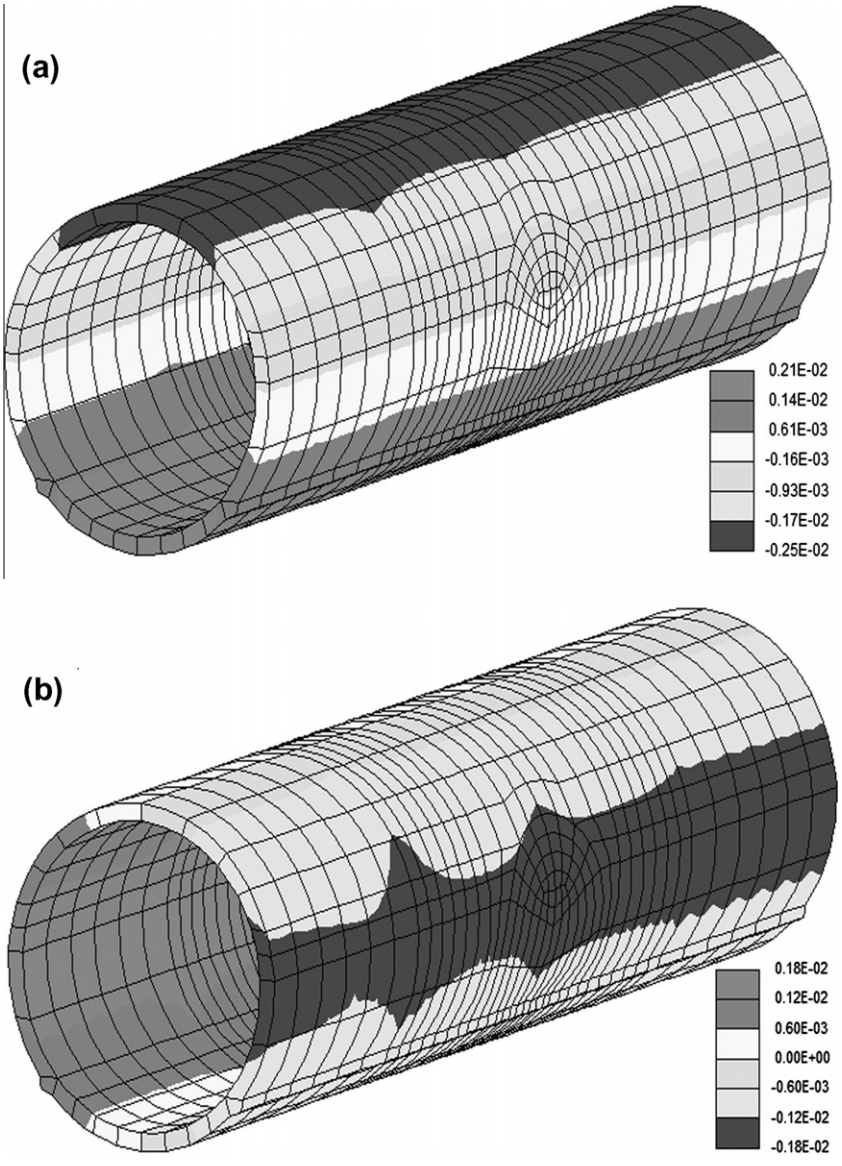


**Figure 7** Deformations for concrete lining (RT). (a) *Z*-direction, (b) *Y*-direction.

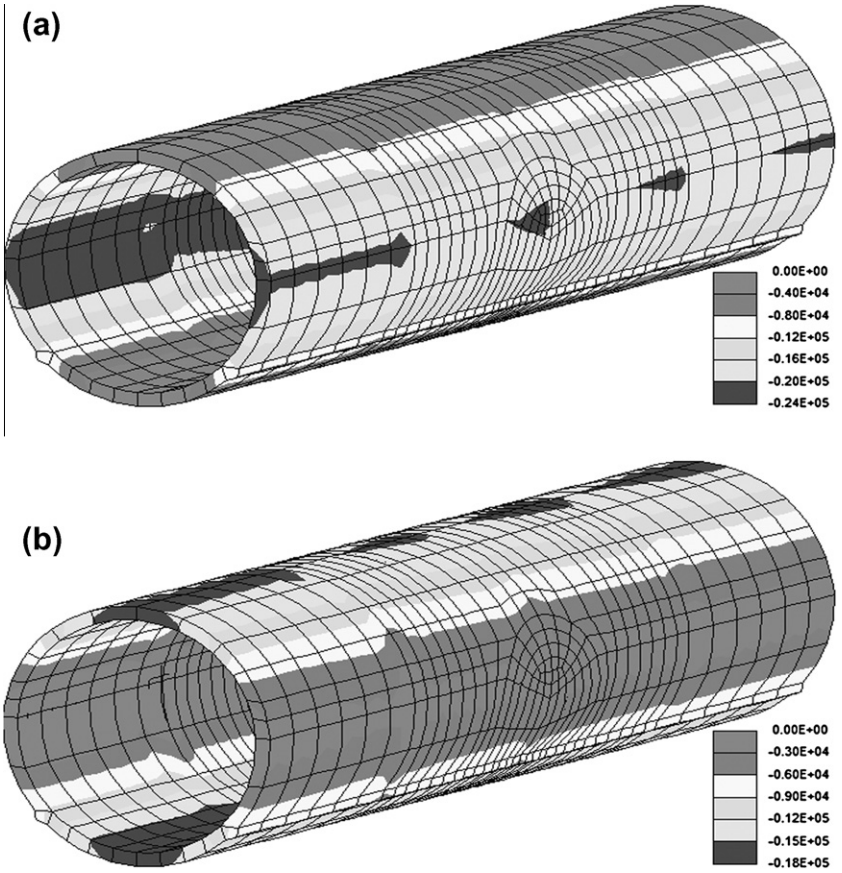


**Figure 8** Resulted stresses for concrete lining (RT). (a) $Z$-stresses $\sigma_Z$ (b), $Y$-stress $\sigma_Y$.

plasticity model based on isotropic work hardening concept [12]. The cross-sections of the loading functions are changing from nearly triangular to nearly circular with increasing hydrostatic pressure (Fig. 1). They have different properties such as symmetry, convexity and smoothness.

The presented code performed the stress–strain relation of concrete under compression stress from the beginning with elastic behavior, followed by a hardening up to the peak-stress and a post-peak perfect plastic behavior. In the developed model, the yield stress has a variable value dependent on the history of the work hardening concept [13].

Finally, the loading surfaces have been formulated with proposing a non-uniform hardening rule based on both a hydrostatic pressure and lode-angle with utilizing the associated flow rule. Each loading surface is defined by a hardening parameter that is a function in the plastic work.

### 3.1. Failure criterion

The failure surface in a general form has been expressed, as:

$$r - r_f(\sigma_m, \theta) = 0 \tag{1}$$

where

$$r = \sqrt{2J_2} = \text{deviatoric length},\ \sigma_m = \frac{1}{3} I_1,\ \theta = \frac{1}{3}\cos^{-1}\left[\frac{3\sqrt{3}}{2} J_3 \Big/ J_2^{\frac{3}{2}}\right] \tag{2}$$

where $\theta$ is the angle of similarity (the lode angle) and $I_1$ is the first invariant. $J_2$ and $J_3$ are the second and third invariants of deviatoric stress tensor, respectively.

The failure formulation ($r_f$) of Ottosen model presented in Eq. (1) has been modified to take the form:

$$r_f(\sigma_m, \theta) = \frac{1}{2A}\left[-(B\cdot\cos\theta + C) + \sqrt{(B\cdot\cos\theta + C)^2 - 4A(D\cdot\sigma_m - 1)}\right] \tag{3}$$

where $A$, $B$, $C$ and $D$ are the four material parameters that can be determined from experimental concrete tests (uniaxial compressive strength, uniaxial tensile strength, biaxial compressive strength and triaxial compressive strength).

The presented failure surface has curved meridians with no intersections with the hydrostatic axis, as shown in Fig. 2.

### 3.2. Subsequent yield surface formulation

The initial and subsequent loading surfaces have been expressed in the general form using a controlling factor $k$, as shown in Fig. 3, on condition that:

$$r - k \cdot r_f \leqslant 0 \tag{4}$$

$k$ is a controlling factor that governs both the shape and the size of the subsequent loading surfaces. The controlling factor $k$ has been used as a function of both the hardening parameter $k_o$ and the mean applied stress $\sigma_m$. Formulation of the

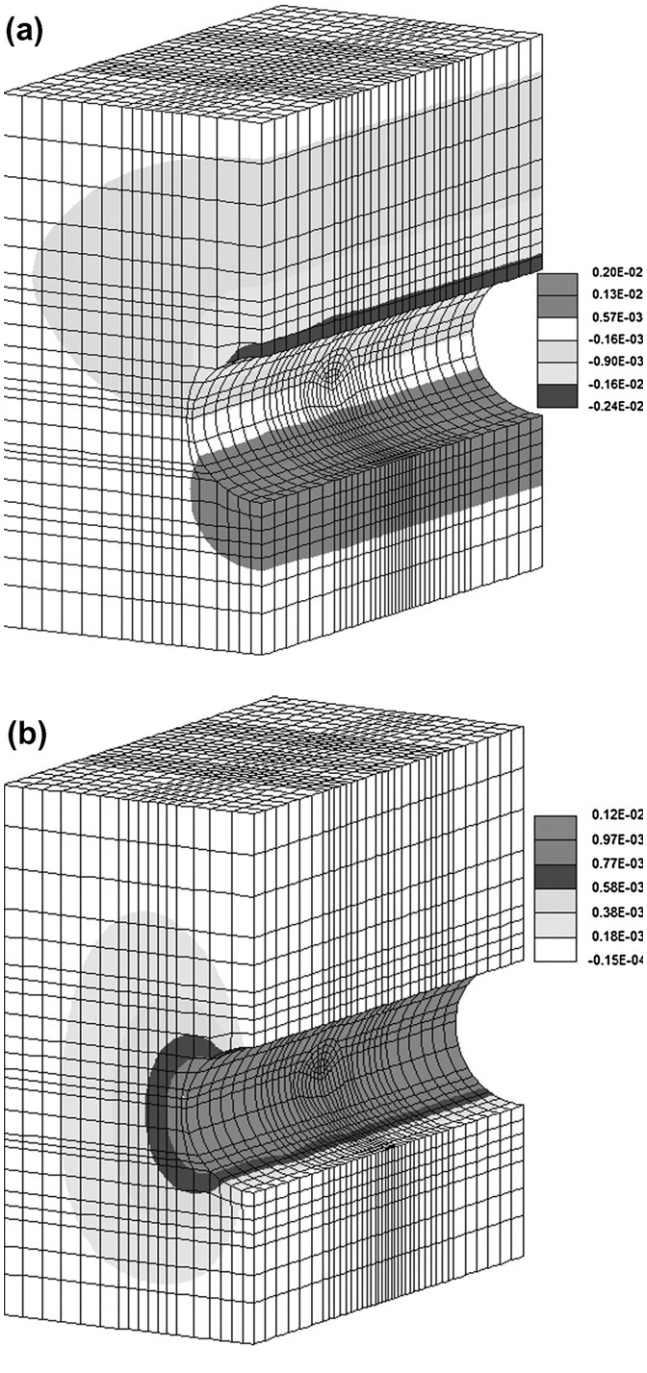


**Figure 9** Deformations for the rock mass (RT). (a) $Z$-direction, (b) $Y$-direction.

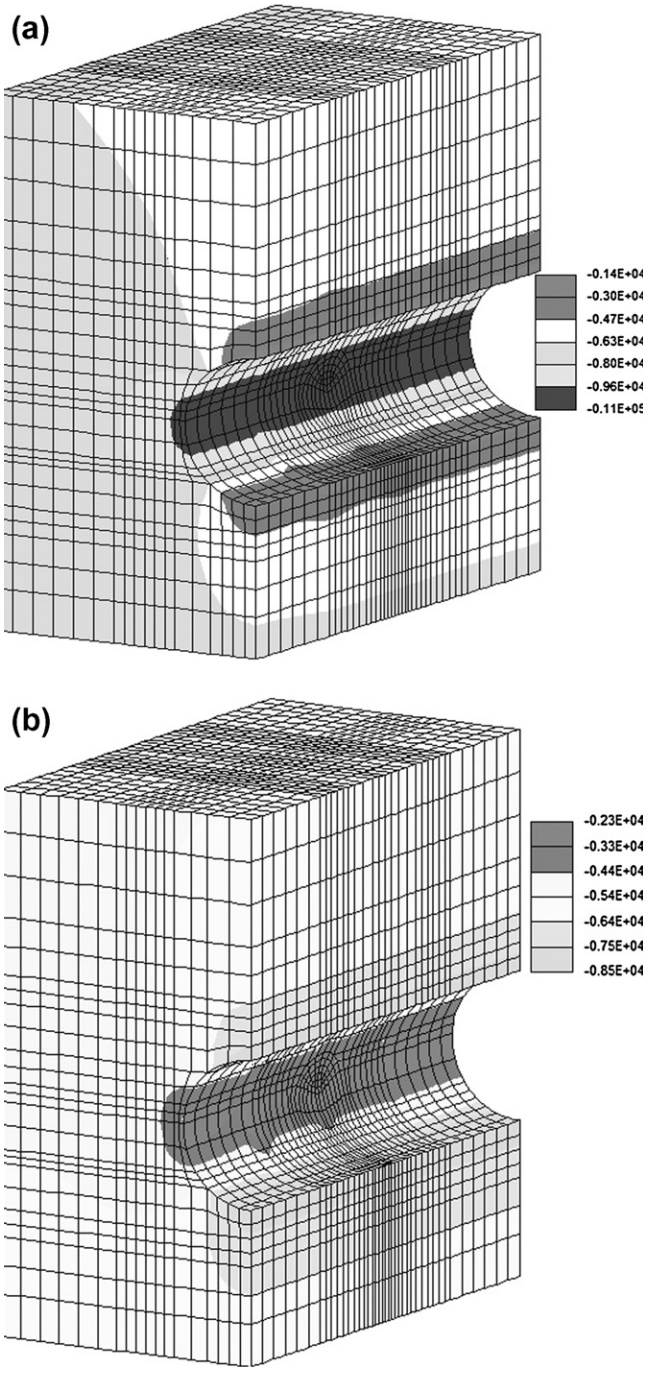


**Figure 10** Resulted stresses for the rock mass (RT). (a) $Z$-stresses $\sigma_Z$, (b) $Y$-stress $\sigma_Y$.

controlling factor, the hardening parameter and the incremental stress-strain relation can be found in [12].

### 3.3. The plastic flow

It was notices that, after initial yielding, the material behaves partly elastic and partly plastic. Therefore, it is assumed that the plastic strain increment $d\varepsilon_{ij}^p$ is proportional to the stress gradient of a quantity termed the plastic potential $g$, and it can be assumed as:

$$d\varepsilon_{ij}^p = d\lambda \frac{\partial g}{\partial \sigma_{ij}} \tag{5}$$

$d\lambda$ is a non-negative scalar function that varies throughout the plastic loading history. The gradient vector $\partial g/\partial \sigma_{ij}$ defines the direction of the plastic strain increment vector. And in case of associated flow role (i.e. $g = F^y$), then the plastic strain increment $d\varepsilon_{ij}^p$ is equal to:

$$d\varepsilon_{ij}^p = \dot{\lambda}^p \frac{\partial F^y}{\partial \sigma_{ij}} \tag{6}$$

where $F^y$ and $\sigma_{ij}$ are the yield function and the stress tensor.

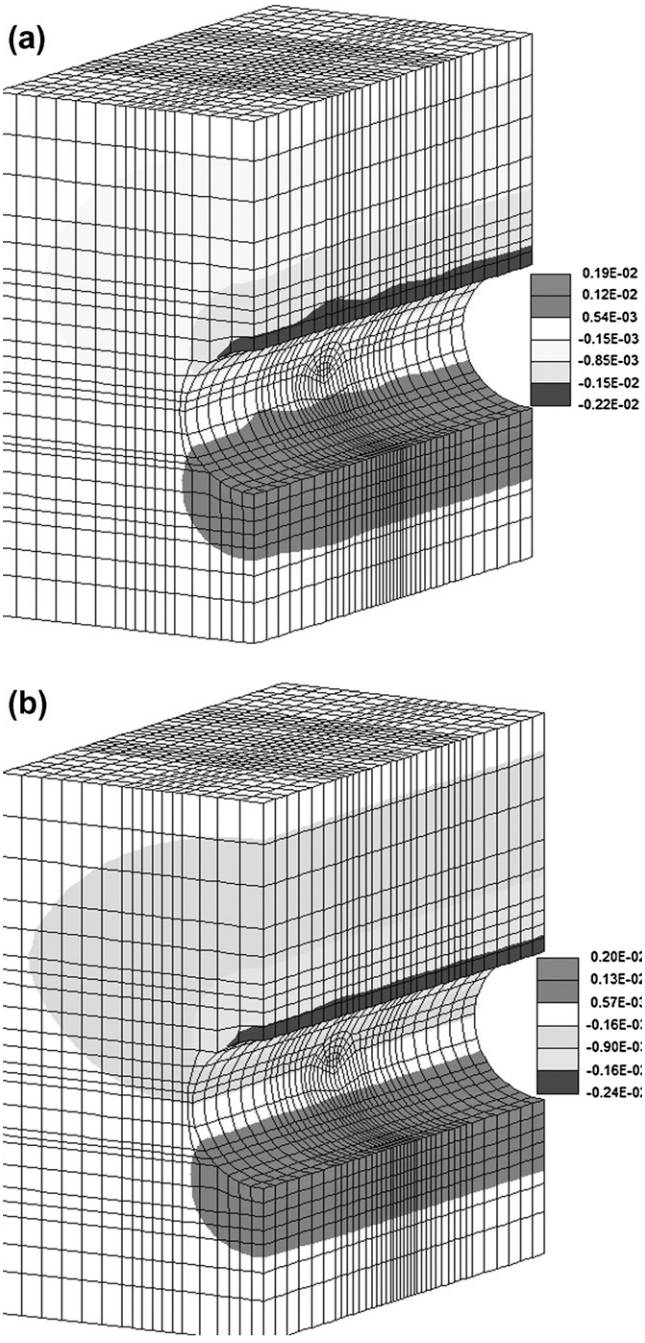


**Figure 11** *Z*-deformations for rock mass for different joint densities. (a) $\omega = 0.0$ (AT1), (b) $\omega = 0.4$ (AT3).

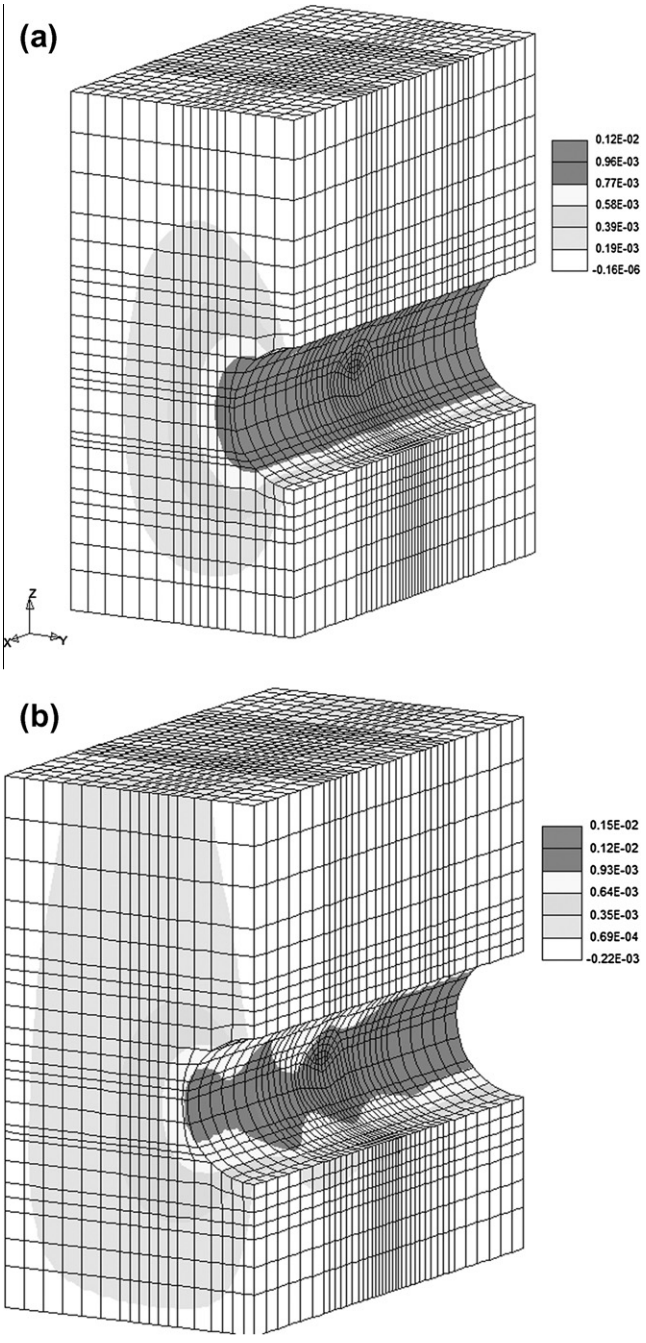


**Figure 12** *Y*-deformations for rock mass for different joint densities. (a) $\omega = 0.0$ (AT1), (b) $\omega = 0.4$ (AT3).

## 4. Calculations for rock mass

In the current work, the plastic formulation of the jointed rock mass has been presented with the deterioration effect on the plastic flow. The formulation of the yield function and plastic response has been introduced in effective stress space as a feasible way to consider the deterioration state (joints configuration) of the jointed rock.

Therefore, to simulate the nonlinear behavior of distortion and failure of rock mass, Mohr–Coulomb criterion with tension cut-off has been adopted in effective stress space (with considering different joint configurations) using simple transformation code [14] from Cauchy stress ($\sigma$) to the effective stress ($\tilde{\sigma}$) by 4th-order transformation tensor [$M$], as follows:

$$\tilde{\sigma}_{kl} = \sigma_{ij} : M^{-1}_{ijkl} \tag{7}$$

The micro-crack transformation tensor has been proposed to be:

$$[M(\Omega)]_{ijkl} = I_{ijkl} - \frac{1}{4}(\delta_{ik}\Omega_{jl} + \delta_{il}\Omega_{jk} + \delta_{ik}\Omega_{il} + \delta_{jl}\Omega_{ik}) \tag{8}$$

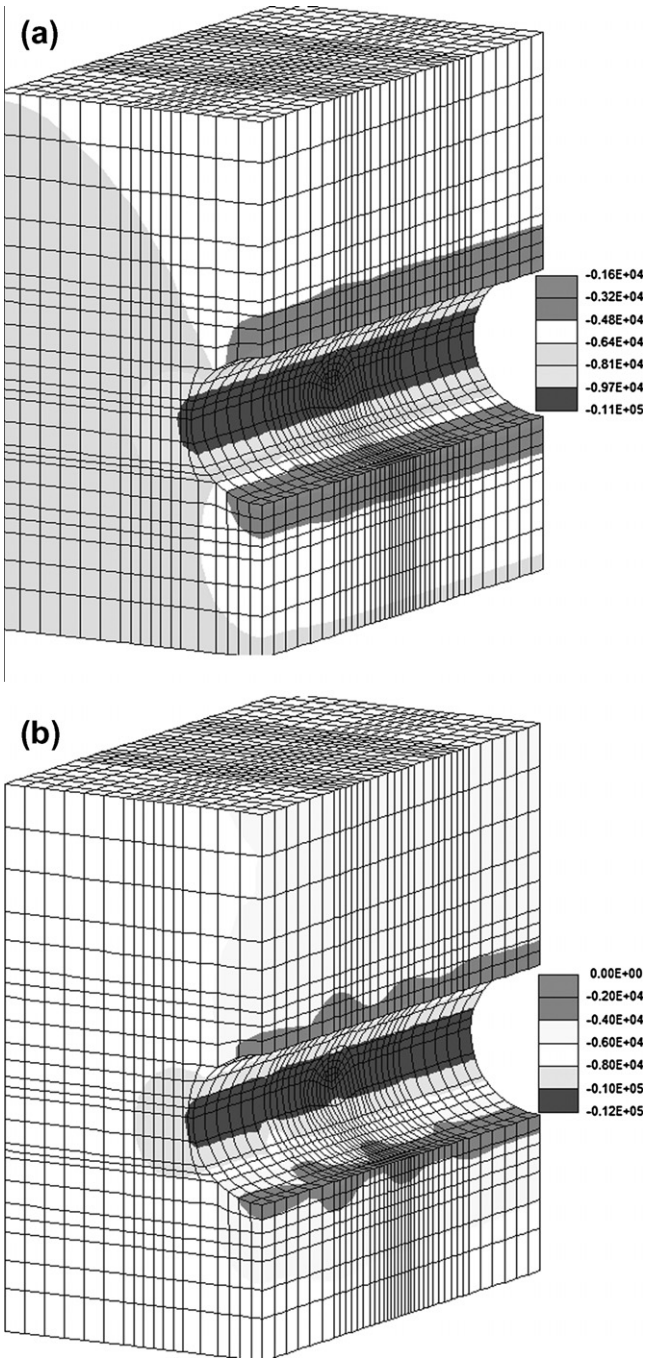


**Figure 13** $\sigma_Z$ for the rock mass for different joint densities. (a) $\omega = 0.0$ (AT1), (b) $\omega = 0.4$ (AT3).

The second-order symmetric damage (joints) tensor $\Omega$ will be presented in a diagonal form and presented by its principal values, as:

$$\overline{\Omega} = \begin{bmatrix} \overline{\Omega}_1 & 0 & 0 \\ & \overline{\Omega}_2 & 0 \\ sym & & \overline{\Omega}_3 \end{bmatrix} \tag{9}$$

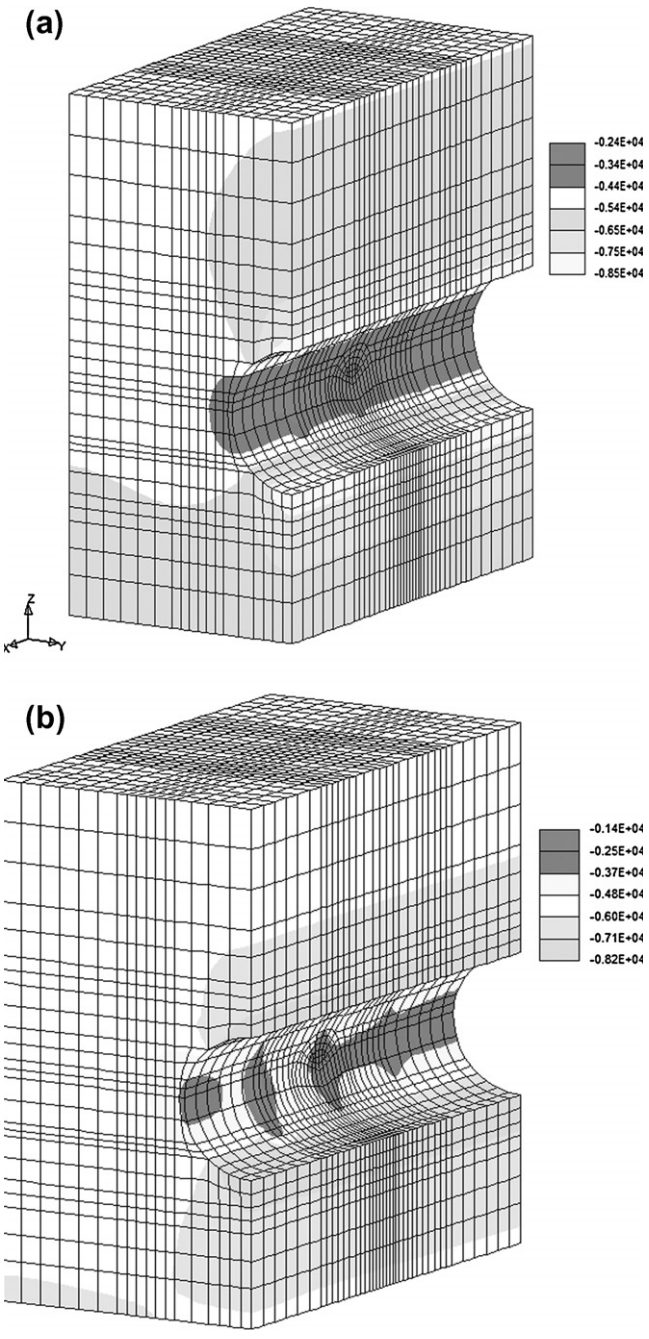


**Figure 14** $\sigma_Y$ for the rock mass for different joint densities. (a) $\omega = 0.0$ (AT1), (b) $\omega = 0.4$ (AT3).

$\overline{\Omega}_i$ represents the principal value of the damage (joints) tensor in the principal direction $i$. Hence, the 4th-order transformation tensor $M(\overline{\Omega})$ will take the following diagonal form, as:

$$[M(\overline{\Omega})] = \begin{bmatrix} 1-\overline{\Omega}_1 & & & & & \\ & 1-\overline{\Omega}_2 & & & & \\ & & 1-\overline{\Omega}_2 & & & \\ & & & 1-\frac{\overline{\Omega}_1+\overline{\Omega}_2}{2} & & \\ & & & & 1-\frac{\overline{\Omega}_1+\overline{\Omega}_3}{2} & \\ & & & & & 1-\frac{\overline{\Omega}_2+\overline{\Omega}_3}{2} \end{bmatrix} \tag{10}$$

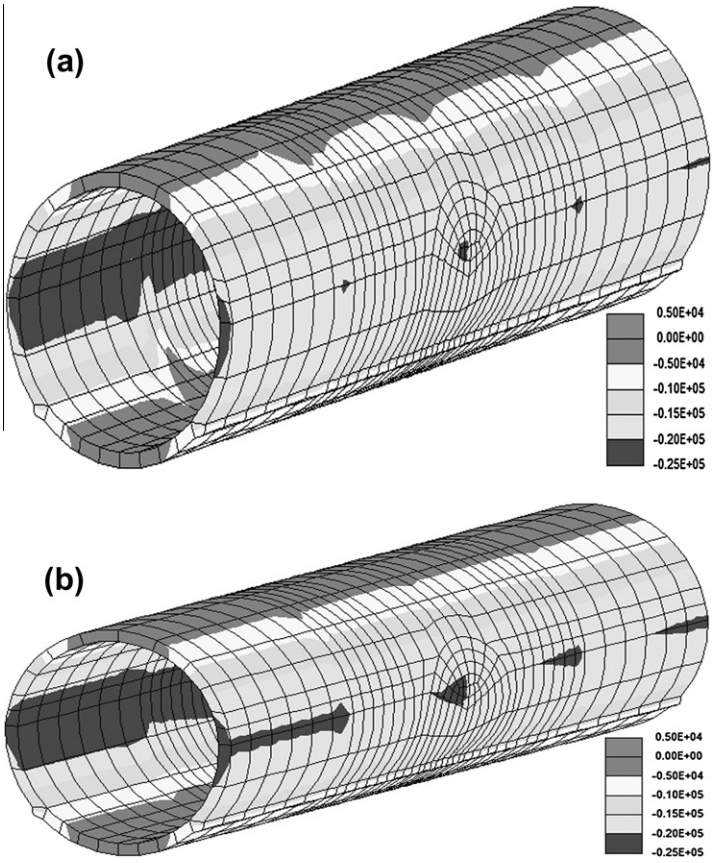


**Figure 15** $\sigma_Z$ for concrete lining for different joint densities. (a) $\omega = 0.0$ (AT1), (b) $\omega = 0.4$ (AT3).

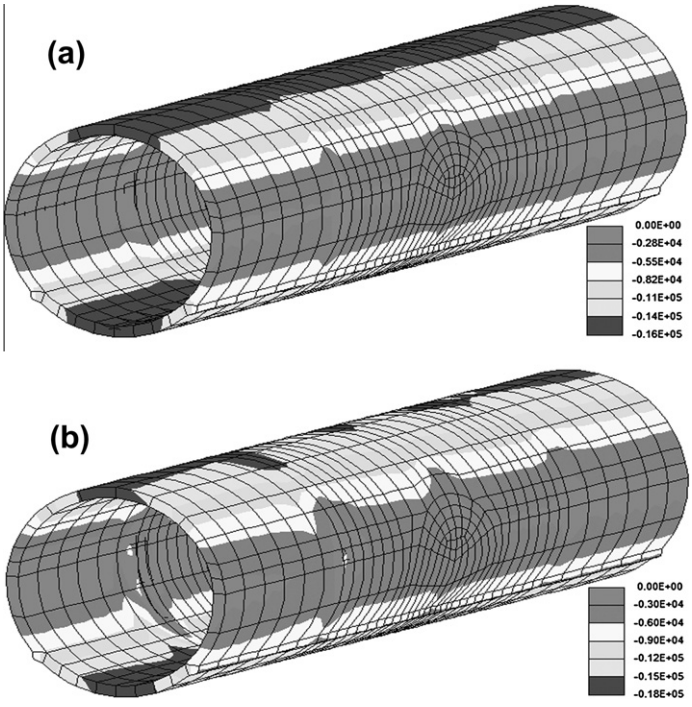


**Figure 16** $\sigma_Y$ for concrete lining for different joint densities. (a) $\omega = 0.0$ (AT1), (b) $\omega = 0.4$ (AT3).

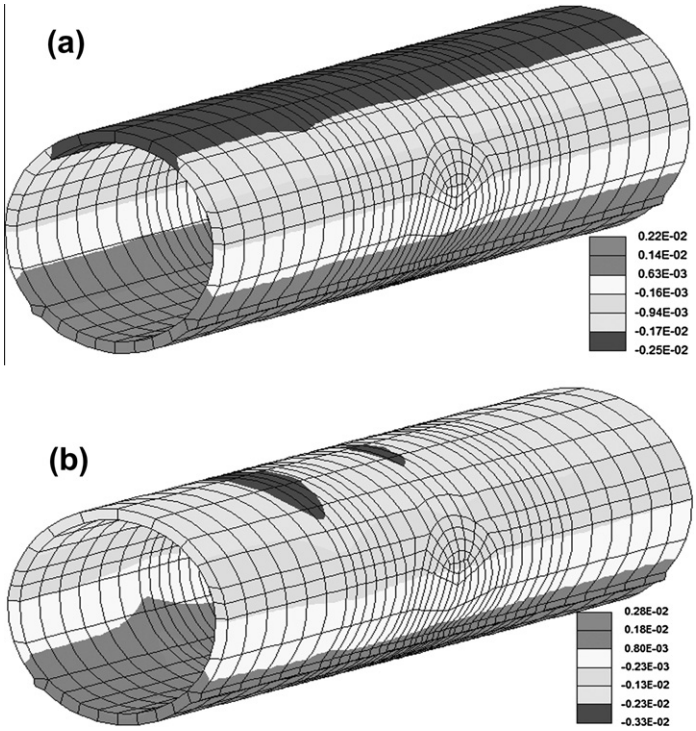


**Figure 17** $Z$-deformations for concrete lining for different joint densities. (a) $\omega = 0.0$ (AT1), (b) $\omega = 0.4$ (AT3).

It is worth mentioning that, within the current elastoplastic formulation the characteristics of the brittle-plastic of rock mass has been simulated considering the joint distribution with their deterioration effect on the plastic flow. The formulation of the yield function and plastic response in effective stress space has been introduced as a feasible way to consider the deterioration state of the rock mass in the plastic calculations [9].

## 5. Joints representation

Presentation of joints has been done by determining joints (damage) tensor using the geological data of a joint set introduced by Swoboda et al. [15]. The orientation of the set of joints is usually identified in the field by sampling alone a line as in a borehole or over an area as on an outcropping surface. The applied joint tensor for rock mass is introduced with three angles of orientations ($\alpha$, $\beta$ and $\gamma$), as shown in Fig. 4. These orientations are related to the dip angle, which is defined by the angle ($\beta$) between the horizontal projection and the line of maximum dip of the joint plane. The dip direction is defined by the angle ($\alpha$) between north and the horizontal projection of the line of maximum dip of the joint plane measured in clockwise direction. And the direction angle ($\gamma$) represents the angle between the tunnel axis and north [15].

In the current numerical investigation, the rock joints have been simulated for simplicity with the same angles of orientations ($\beta = 45°$ and $\gamma = 0°$) which represents a general inclined joint system. For example, the resulting 2nd order joint tensor for rock mass with joints density $\omega = 0.1$ with dip angle $\alpha = 90°$ will be:

$$\Omega_{in}(rock) = \begin{bmatrix} 0 & 0 & 0 \\ 0 & 0.05 & -0.05 \\ 0 & -0.05 & 0.05 \end{bmatrix} \tag{11}$$

It is worth mentioning that the joints in rock mass in the current analysis have been considered in a passive status (i.e. no evolution or propagation).

## 6. Proposed numerical test program

The current numerical investigation has been carried out using the material properties listed in Table 1.

Three numerical groups are considered, as listed in Table 2. For comparison, one additional tunnel case (RT) has been considered as a reference tunnel case.

For each case, Table 2 lists the tunnel depth, the joint density ($\omega$) and the joint orientations ($\alpha°$). In Group A, the joint density has been changed with three different values ($\omega = 0.0$, 0.2 and 0.4), respectively. The tunnel depth has been altered with different five values in Group B. The investigated parameter in Group C is the orientation of rock joints ($\alpha°$) taking two values (0° and 45°).

## 7. Verification of the proposed numerical model

To verify the proposed numerical investigation, the Brenner-Base tunnel in the Alps at the border between Austria and Italy. This tunnel is one of the most important traffic connections between northern and southern Europe.

The origin of the coordinate system is on the intersection line of the two symmetry planes and the $X$-direction points

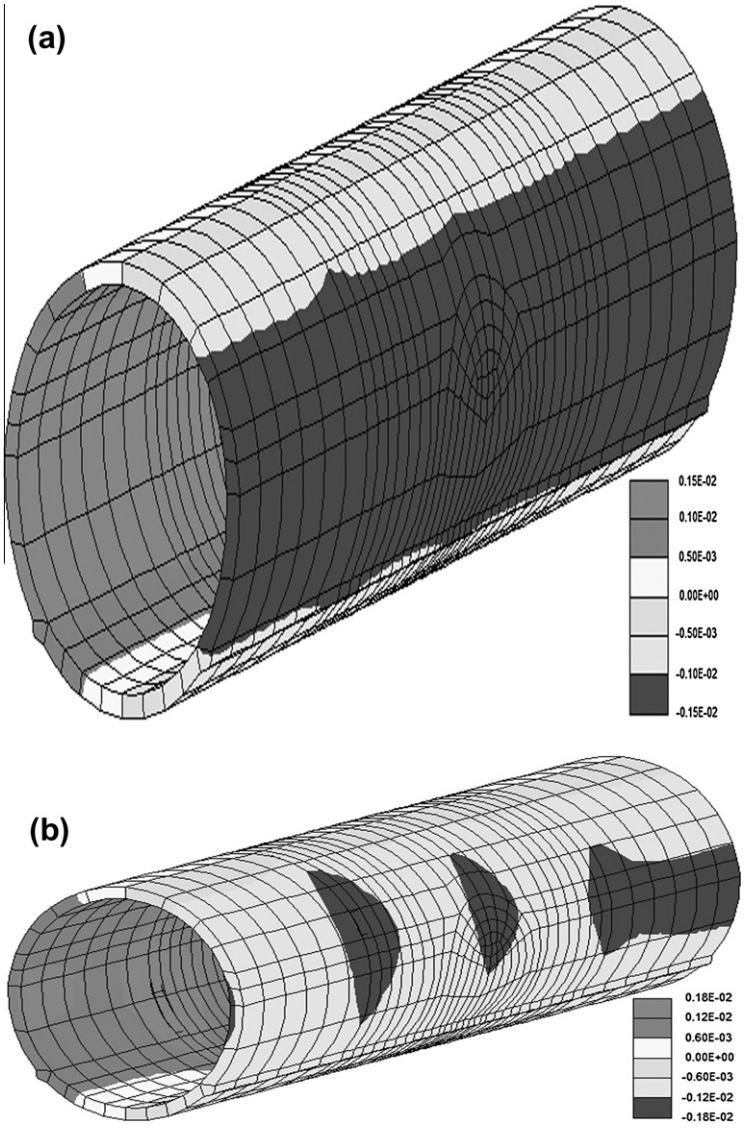


**Figure 18** *Y*-deformations for concrete lining for different joint densities. (a) $\omega = 0.0$ (AT1), (b) $\omega = 0.4$ (AT3).

toward the main tube, the *Y*-axis toward the transverse direction and the *Z*-axis is upward, as shown in Fig. 5a.

The current investigation has focused on the main tunnel without any excavation steps for the intersection tube. The main tunnel has been excavated in four main construction steps. The partial excavation and shotcrete of the different parts of the tunnel are simulated in different loading steps. After the excavation process for any part, the concrete lining with thick 50.0 cm is inserted to the inner face of this part of the tunnel assuming perfect contact between rock and concrete lining (i.e. there is no interface between the two materials). The finite element mesh of the tunnel was generated by the pre-processor program ANSYS [16]. The thickness of the concrete lining remained unchanged within the current numerical investigation in order to investigate the influence of the concerned parameters (joints orientation, joints density and tunnel depth) on the stability of tunnel excavated in jointed rock mass to avoid any external influence of the supporting role of the concrete lining on the excavation process.

The finite element mesh for the tunnel is composed of nearly 34,000 Isoparametric Quadratic Solid elements (20 nodes), as displayed in Fig. 5b. The cross section of concrete lining of the main tunnel for all models has a circular profile, as shown in Fig. 5c.

## 8. Loading and excavation process

### *8.1. Initial loading step*

The primary state of stress is the initial stress field in the ground, before tunnel excavation process. This initial stress state can be considered either over the dead weight of rock or by applying the initial stress loads. In deep tunnels, the whole elements are stressed with the initial stress method. The initial stress field has three components; the vertical stresses $\sigma_z$ can be computed from Eq. (12). The two other horizontal stresses $\sigma_y$ and $\sigma_x$ are due to the unknown load history of the low-lying rock which can be evaluated by a lateral earth

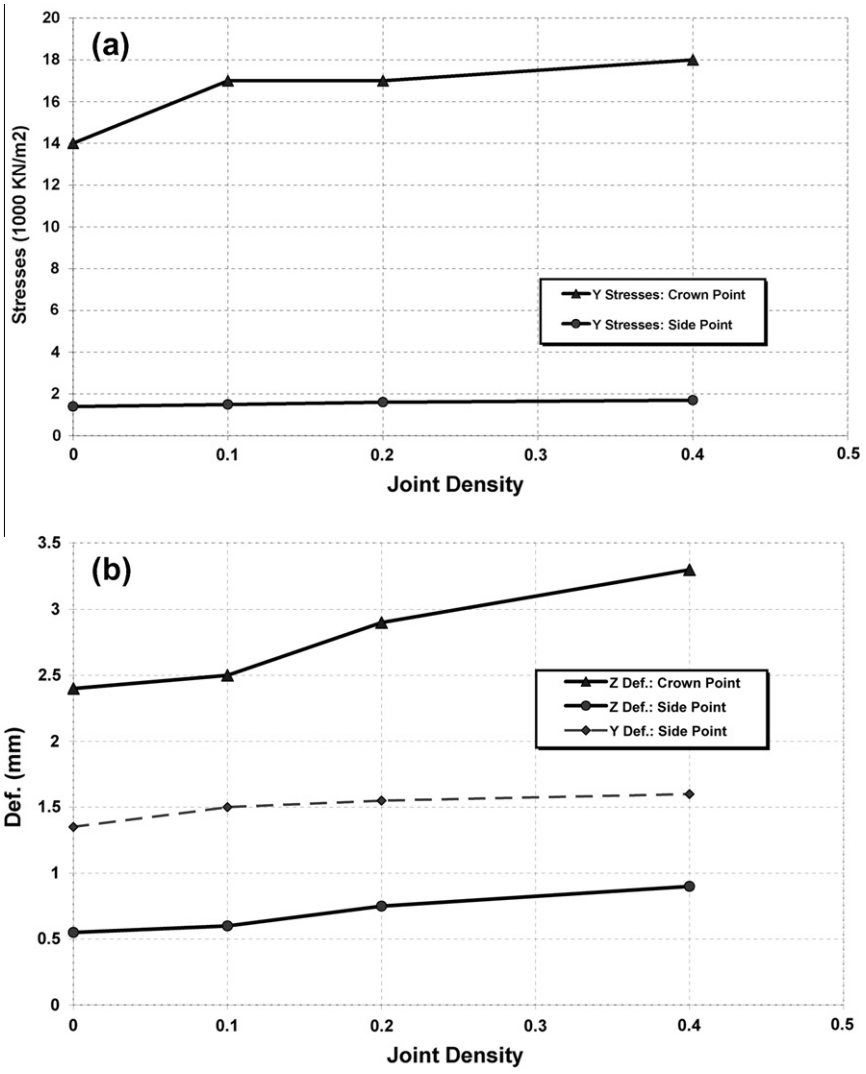


**Figure 19** Impact of joints density to concrete lining. (a) Resulted stresses, (b) obtained deformations.

pressure coefficient $k_Z$ that has been taken 0.8 for the current numerical investigation, as shown in Eq. (13).

$$\sigma_z = \lambda_z \cdot h \tag{12}$$

$$\sigma_x = \sigma_y = k_Z \cdot \sigma_z \tag{13}$$

The bulk unit ($\lambda_Z$) is the weight of the rock and $k_Z$ is the coefficient of lateral earth pressure at rest.

### 8.2. Excavation process

The excavation process has been done in four main stages. Each stage contains the followings:

- The loosen state of the rock mass that has been done in two sub-steps by decreasing the modulus of elasticity until reaching zero representing the excavated state.
- The hardening process of the concrete lining that has been considered also in two sub-steps by increasing the modulus of elasticity until reaching the maximum value of concrete materials.

For the simulation of the excavation process, the excavated elements have been deleted, whereby this will change the loading state. This change has been computed using FINAL program [17] with the stress elimination method. The resulted tension stresses of the deleted elements converted and set as external nodal forces on the surrounding element nodes. The tension stresses which arise as a result of the redistribution of stresses were applied to the excavated cross section of the surrounding elements.

## 9. Analysis and discussions

To monitor the effect of the investigated parameters on the cross-sectional deformations and stresses, two key points have been chosen on the perimeter of the concrete lining (the crown and the side points) at the tunnel face, as shown in Fig. 6.

Table 3 presents the numerical results for these two main points (the crown and side points) of the concrete lining. These results represent the average values of the numerical results of

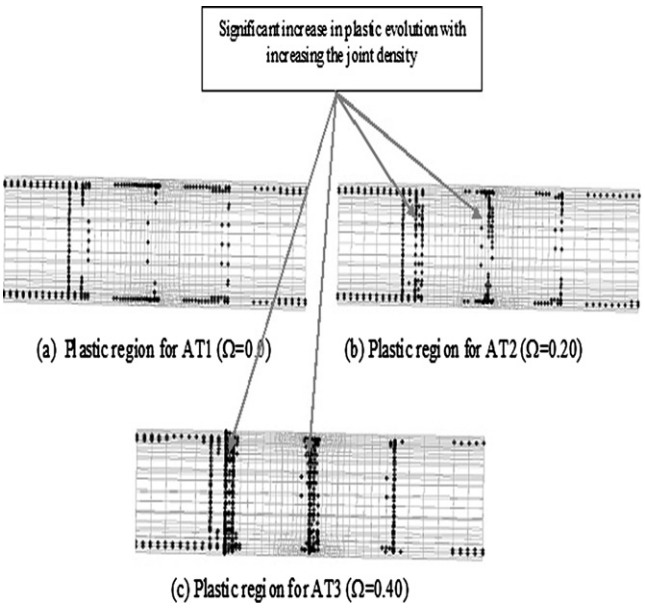


**Figure 20** The impact of joint density to plastic distribution.

all points through the concrete thickness (50 cm) at these critical sections.

The resulted graphic outputs are shown from Figs. 7–39. The introduced results for the numerical calculation are presented for all tunnel cases after the full excavation process.

Figs. 7–10 show the resulted deformations and stresses in $Z$ and $Y$ directions for the reference tunnel model (RT) for both concrete lining and the surrounding rock mass.

As a general result for all numerical models, the induced deformations and the differences in stresses for all cases (concrete lining and surrounding rock mass) are relatively small. This result may be interpreted because of different reasons such as; the thickness of concrete lining (50 cm), the high grade of the used shotcrete and the good quality of surrounding rock. In addition, the stiff concrete lining significantly resists the external loads and plays an effective supporting role for the surrounding rock mass.

The effect of the different factors on the tunnel stability can be analyzed, as follow:

## 10. With respect to joints density

### *10.1. Impact to rock mass*

The impact of joints density to the rock mass for the deformations and the stresses distributions ($Z$ and $Y$ directions) are introduced in Figs. 11–14.

Deterioration due to rock joints leads to a reduction of the loading carrying area with inducing stress concentration around the defects, as presented in Eq. (7).

Therefore, by increasing the rock joint density ($\omega$), a slight increase in the deformations of the rock mass is obtained in both $Z$ and $Y$ directions (Figs. 11 and 12). These results could be obtained due to the good quality of the surrounding rock mass used in the current analyses. And the stable rock conditions that may effectively close the rock joints. In addition, the

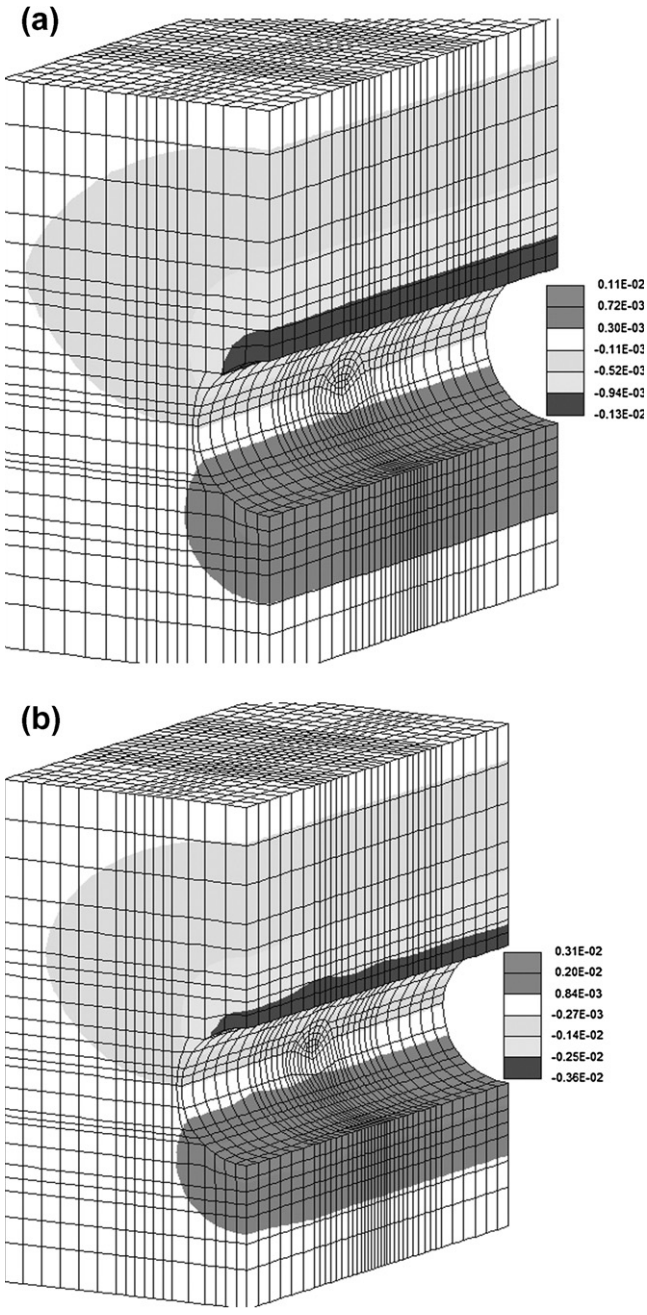


**Figure 21** $Z$-deformations for rock mass for different tunnel depths. (a) Depth = 300.0 m (BT2), (b) depth = 600.0 m (BT4).

stiff concrete lining provides an effective supporting role to the surrounding rock mass as well.

Figs. 13 and 14 show a clear increase in the resulted stresses induced around the tunnel. Such increase may be obtained from the stresses concentration around the rock joints with increasing the joints density which consequently magnifies the obtained stresses.

### *10.2. Impact to concrete lining*

The displayed numerical results in Table 3 for RT and Group A show no clear effect of the rock joint density on the obtained

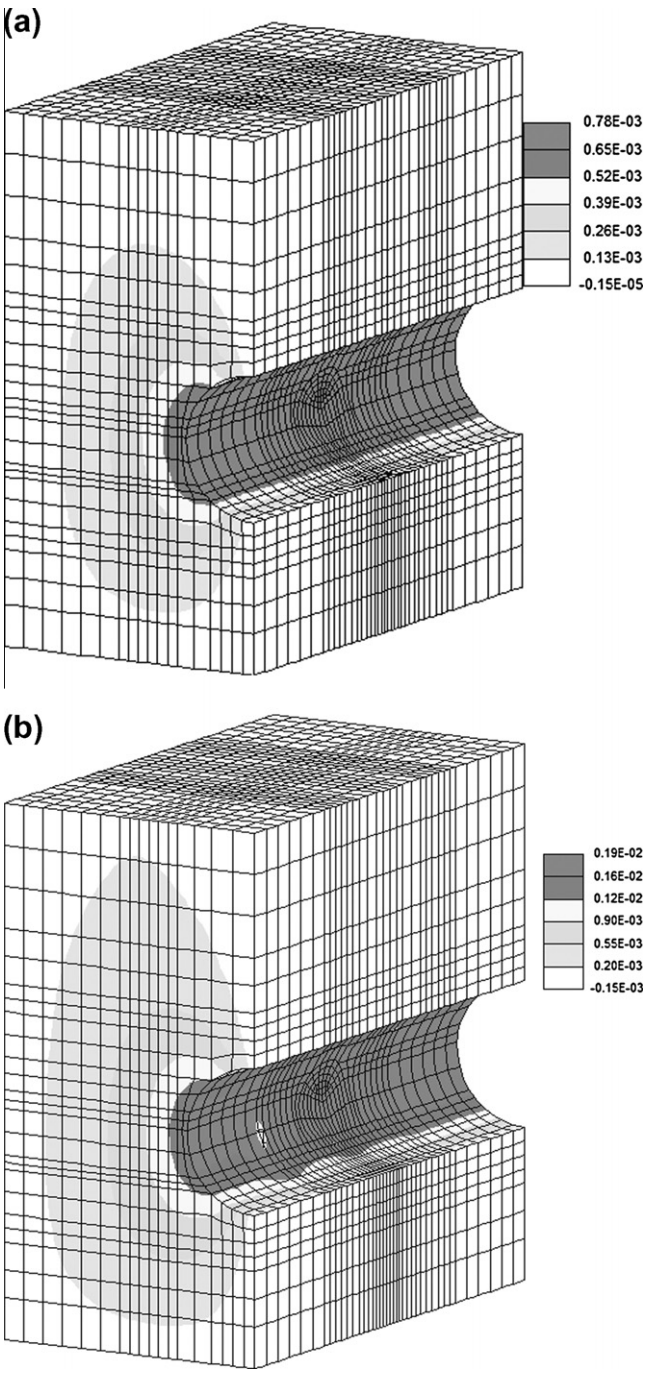


**Figure 22** *Y*-deformations for rock mass for different tunnel depths. (a) Depth = 300.0 m, (BT2) (b) depth = 600.0 m (BT4).

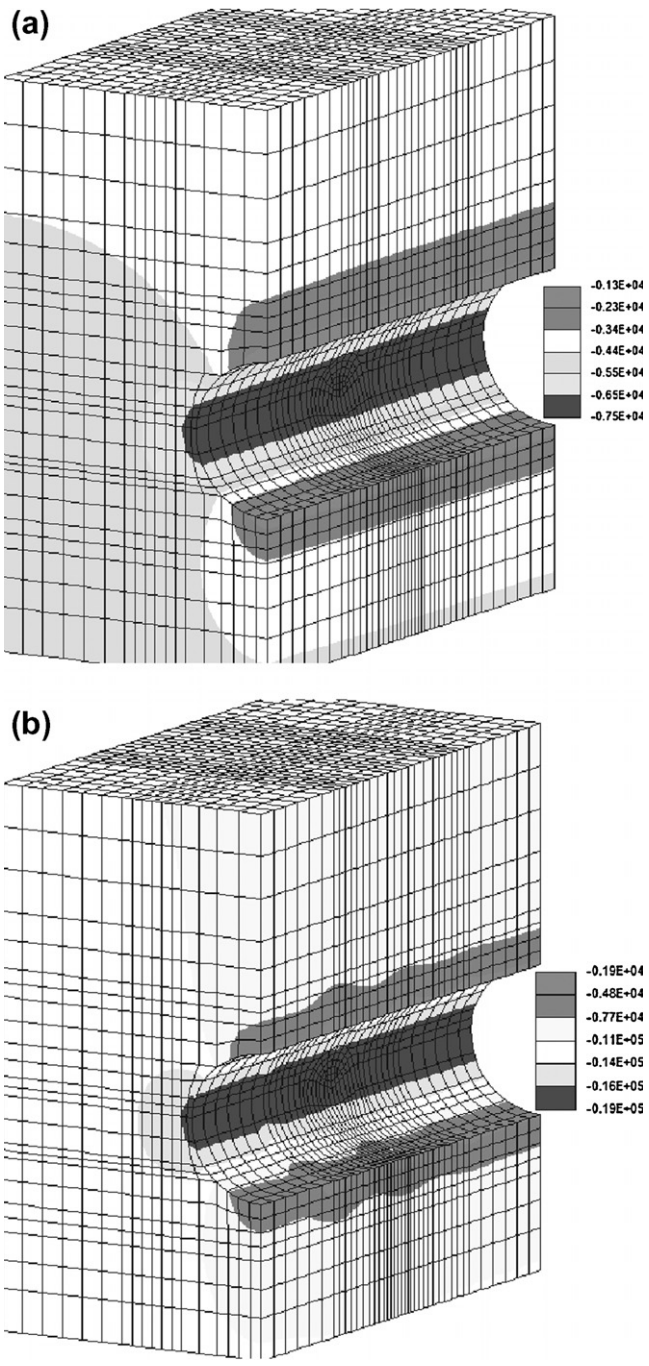


**Figure 23** $\sigma_Z$ for rock mass for different tunnel depths. (a) Depth = 300.0 m (BT2), (b) depth = 600.0 m (BT4).

*Z*-stresses (see Fig. 15). However, a slight increase in the *Y*-stresses of the concrete lining can be found in Fig. 16. These results may be appeared due to the induced high compressive stresses that may close the rock joints. Beside, the non-propagation assumption of the joints that has been proposed through the current numerical investigation, in addition to the stable confinement conditions presented by the good quality of the used rock mass to the concrete lining.

Table 3 and Fig. 19a show that, the rock joints have a clear influence on the resulted *Y*-stresses and no impact to *Z*-stresses. This influence could be a result of the obtained tensile stresses resulted from the excavation process, besides the arch action of the circular profile of the tunnel cross section which increase the *Y*-stresses significantly.

Figs. 17 and 18 introduce the effect of joint density on the resulted deformations of the concrete lining. It is obvious that the impact of joint density on the *Z*-deformations (Fig. 17) is higher than that for the *Y*-directions (Fig. 18).

The obtained cross-sectional deformations are presented in Fig. 19b for the tunnel face. It is obviously that the increase in the deformations of the Crown Point has the same trend for

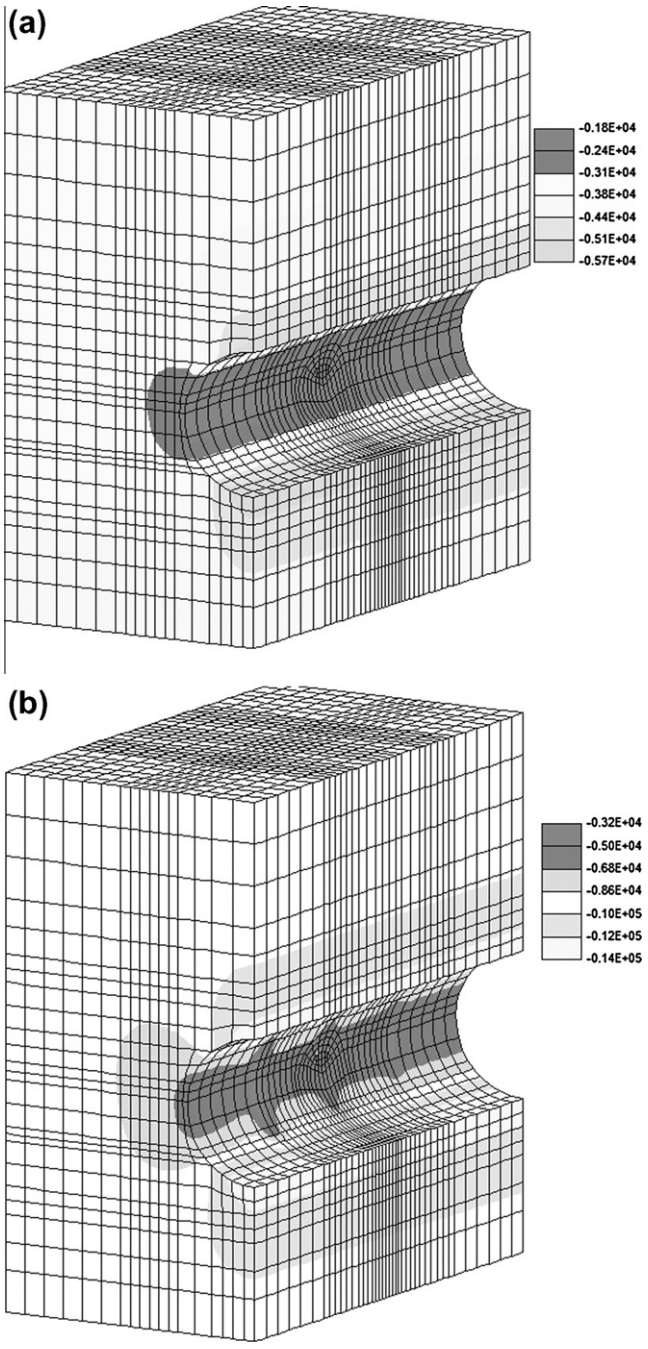


**Figure 24** $\sigma_Y$ for rock mass for different tunnel depths. (a) Depth = 300.0 m (BT2), (b) depth = 600.0 m (BT4).

the side point but with higher rate in case of $Z$-deformations. For the $Y$-direction, the side point has a clear increase with increasing the joint density.

Furthermore, the impact of the joint density to the creation and evolution of the plastic regions is displayed in Fig. 20. This result agrees with the reinforcing impact of existence damage (rock joint) on accelerating the initiation and evolution of plastic flow [18]. The plastic region concentrates on the top and bottom inner face of the concrete lining due to the resulted tensile forces obtained from the excavation process.

## 11. With respect to tunnel depth

The impact of the tunnel depth on rock mass and the concrete lining for different tunnel cases included in Group B is introduced in Figs. 21–28.

### *11.1. Impact to rock mass*

The intensive increase in $Z$ and $Y$ deformations with increasing the tunnel depth is displayed in Figs. 21 and 22, respectively. The increase in the obtained results in case of the $Z$ deformations have the same trend but with higher values than that in case of the $Y$ deformations.

Figs. 23 and 24 show the gradual increase in the vertical and horizontal induced stresses around the tunnel opening with increasing the tunnel depth. Meanwhile, there is an intensive growth in the compression stresses up to the borders of the rock mass. This could be resulted from the increase in the overburden pressure with increasing the tunnel depth. Also, the compression zones around the tunnel tube have nearly the same trend but the corresponding values dramatically evolve with increasing the tunnel depth. This may be interpreted because of the stable supporting conditions introduced by the concrete lining.

### *11.2. Impact to concrete lining*

For concrete lining, Figs. 25–28 show the obtained deformations and stresses for different tunnel depths included in Group B.

From the deformations point of view, Figs. 25 and 26 show a significant increase with increasing the tunnel depth. This increase corresponds to the higher overlaying rock mass over the concrete lining. The values of the maximum deformations in the Crown Point increased rapidly more than that for the side point in case of $Z$-deformations, as displayed in Fig. 29a.

For the tunnel face, the increasing rate for $Z$-deformations for the Crown Point is almost linear with increasing tunnel depth. In case of the $Y$-deformations, the obtained values for the side point are increasing dramatically more than that of the $Z$-deformations for the same point at the same tunnel depth, as monitored in Fig. 29a. These results may be attributed to the arch action impact with the circular tunnel profile.

As a general result, there is a clear increase in the induced stresses ($\sigma_z$ and $\sigma_y$) for the concrete lining with increasing the tunnel depth, as shown in Figs. 27 and 28, respectively.

Also, it appears that the impact of the tunnel depth to the side point is higher than for the Crown Point in case of $Z$-stresses but this influence is reversed in case of $Y$-stresses. Also, by increasing the tunnel depth, the $Z$-stresses for the side point and $Y$-stresses for the Crown Point increase dramatically in a nearly linear rate with increasing the corresponding compression zones.

In Fig. 29a, the increasing rate of the resulted deformations for both $Z$ and $Y$ directions for the side point decreases with increasing the tunnel depth. Also, very slight increase for both $Z$-stresses for the Crown Point and $Y$-stresses for the side point is observed with increasing the depth, as displayed in Fig. 29b. There is nearly no increase in the induced stresses after tunnel depth 600 m and the relation with the tunnel depth becomes almost constant. These results may be explained because of

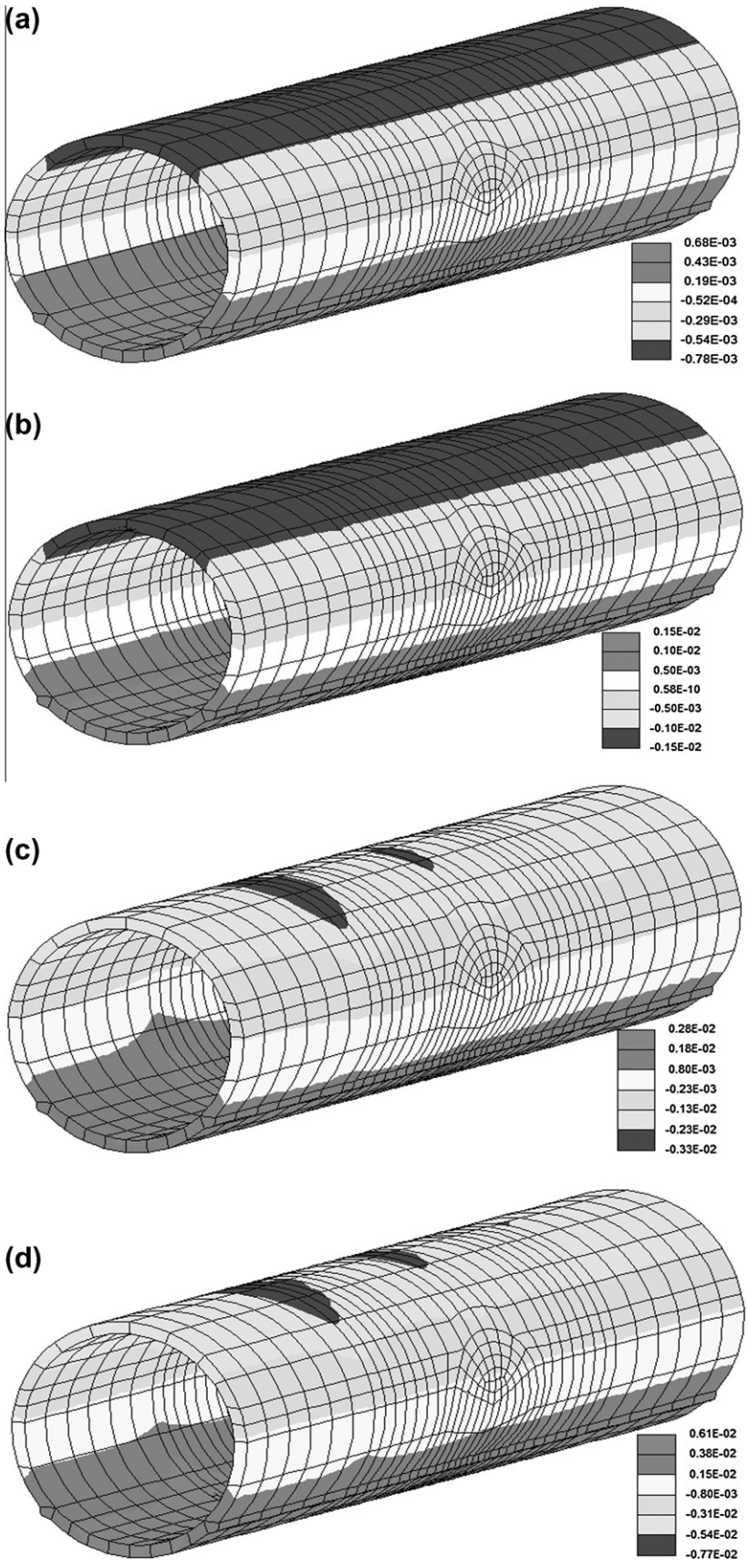


**Figure 25** *Z*-deformations for concrete lining for different tunnel depths. (a) Depth = 200.0 m (BT1), (b) depth = 300.0 m (BT2), (c) depth = 600.0 m (BT4) (d) depth = 800.0 m (BT5).

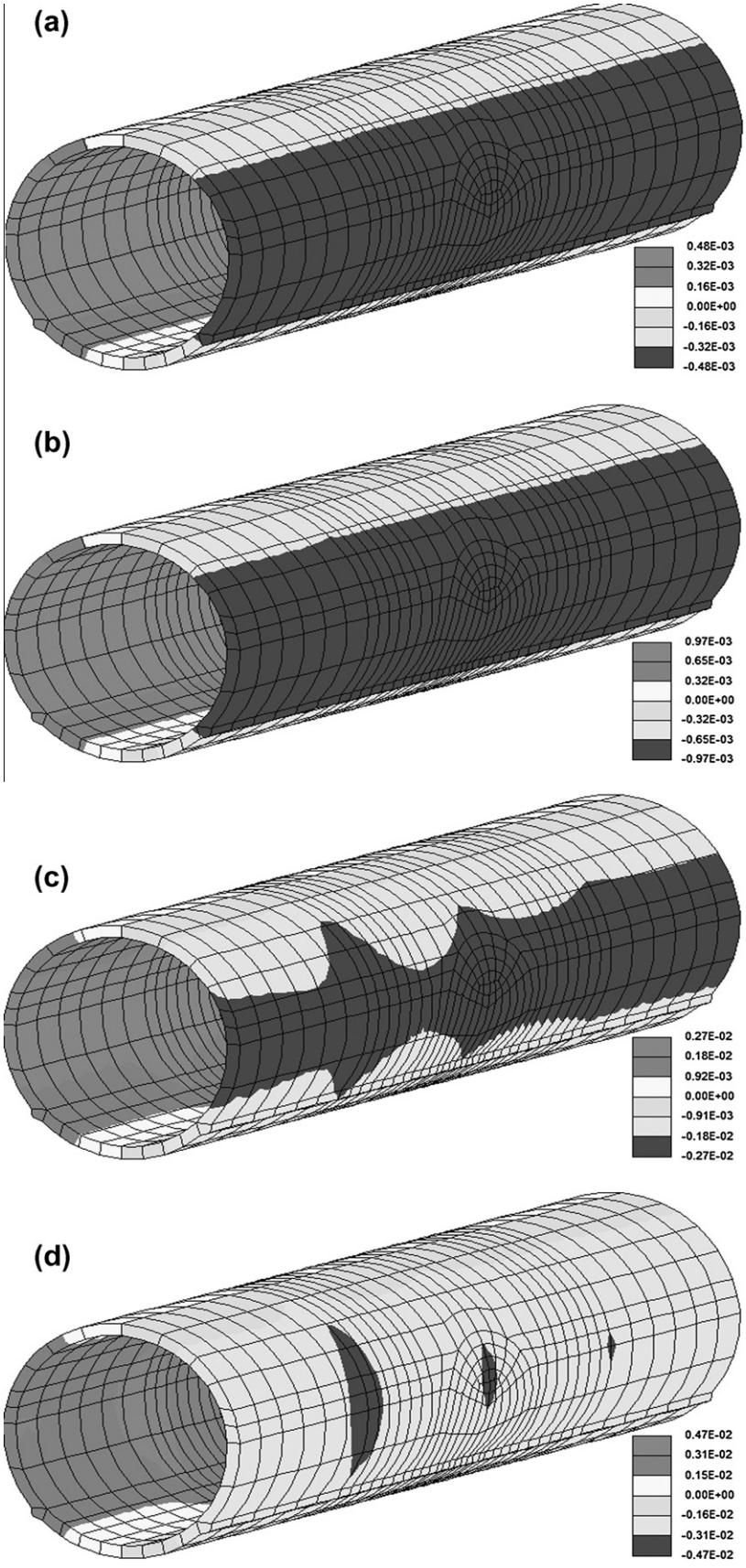


**Figure 26** *Y*-deformations for concrete lining for different tunnel depths. (a) Depth = 200.0 m (BT1), (b) depth = 300.0 m (BT2), (c) depth = 600.0 m (BT4), (d) depth = 800.0 m (BT5).

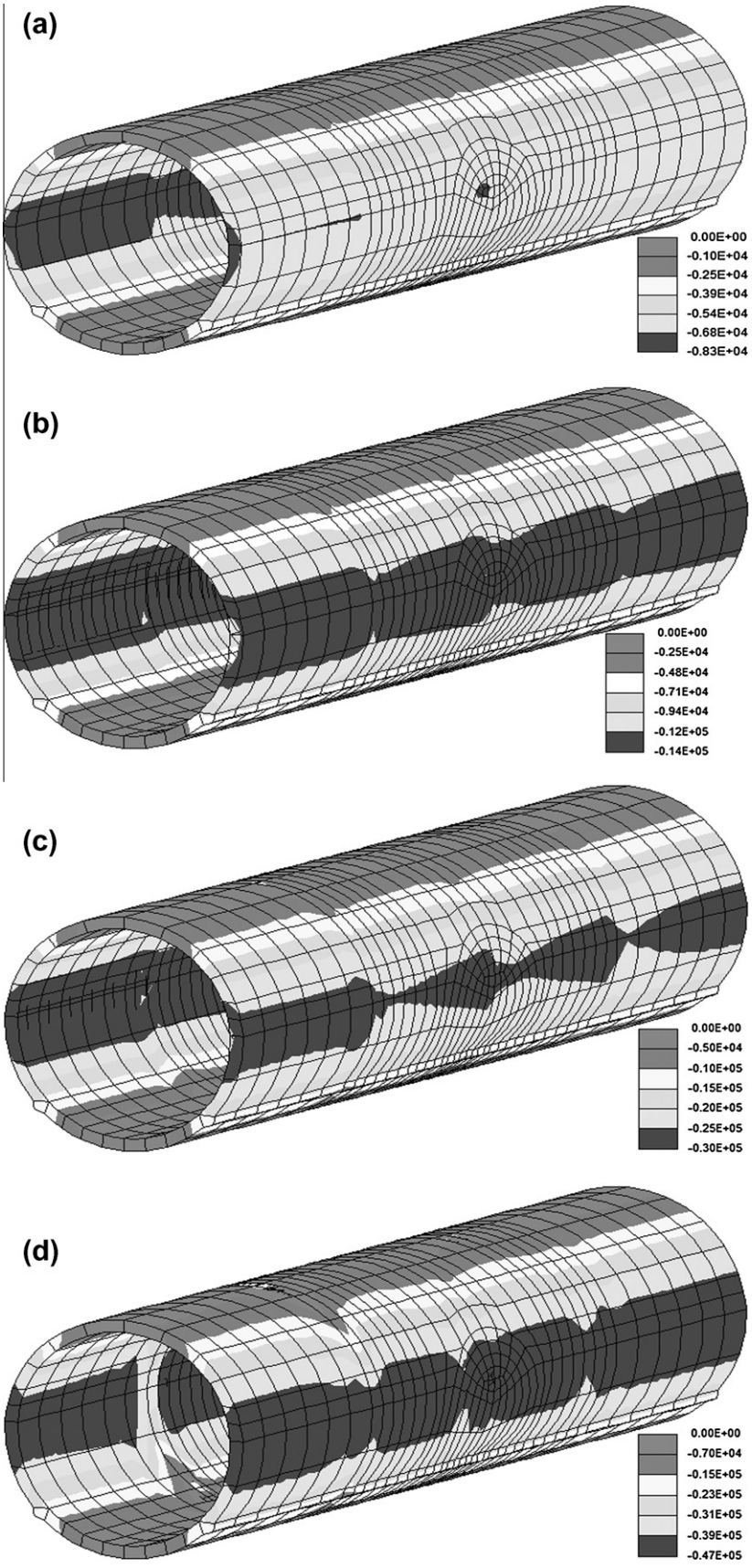


**Figure 27** $\sigma_Z$ for concrete lining for different tunnel depths. (a) Depth = 200.0 m (BT1), (b) depth = 300.0 m (BT2), (c) depth = 500.0 m (BT3), (d) depth = 800.0 m (BT5).

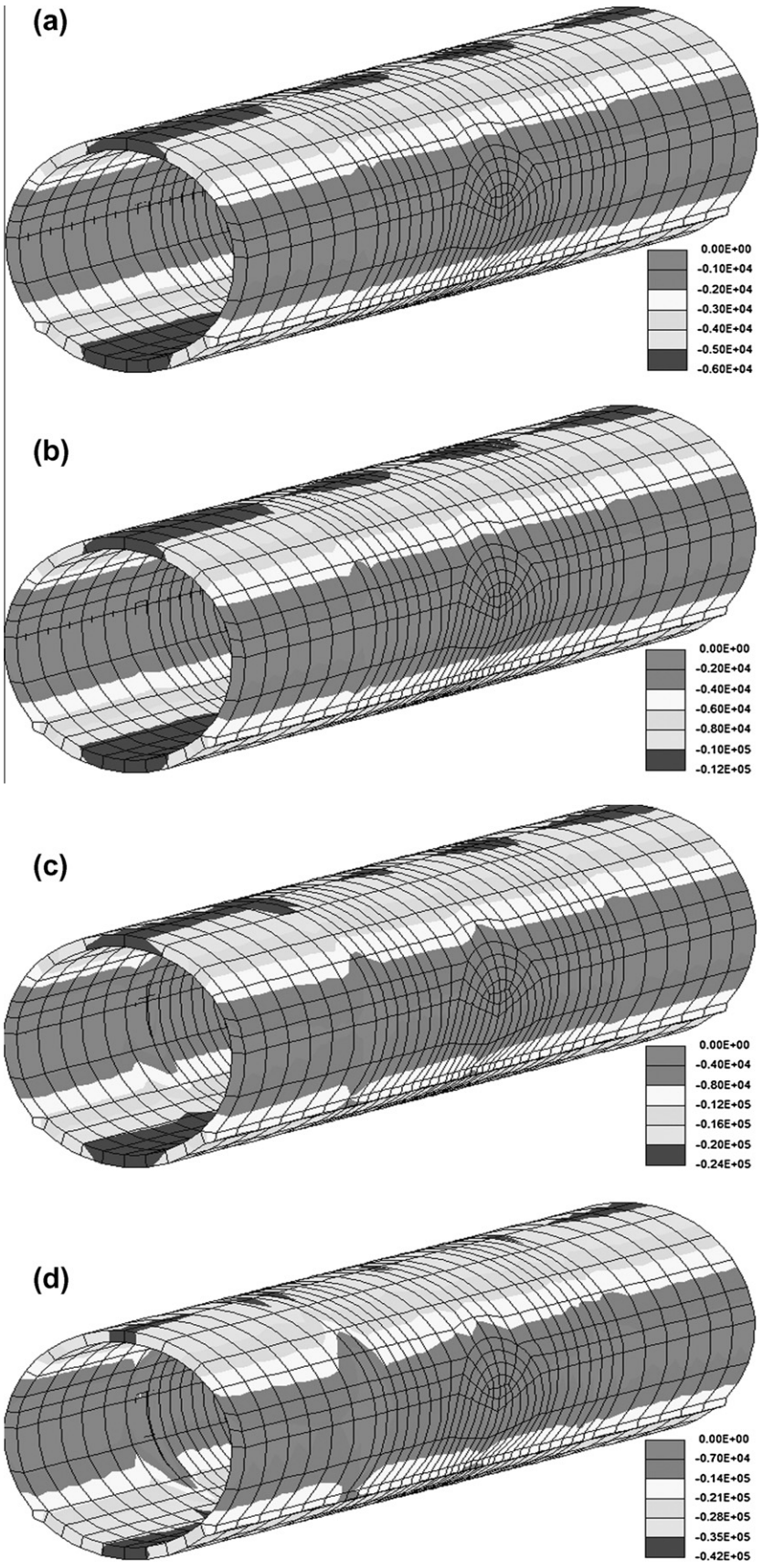


**Figure 28** $\sigma_Y$ for concrete lining for different tunnel depths. (a) Depth = 200.0 m (BT1), (b) depth = 300.0 m (BT2), (c) depth = 500.0 m (BT3), (d) depth = 800.0 m (BT5).

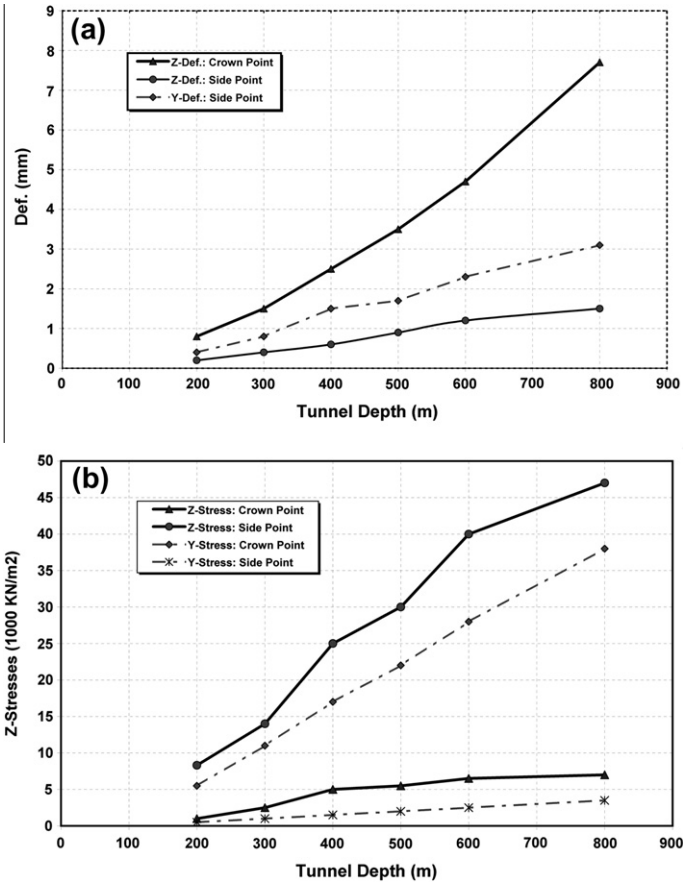


**Figure 29** Impact of tunnel depth for concrete lining. (a) Obtained deformations, (b) resulted stresses.

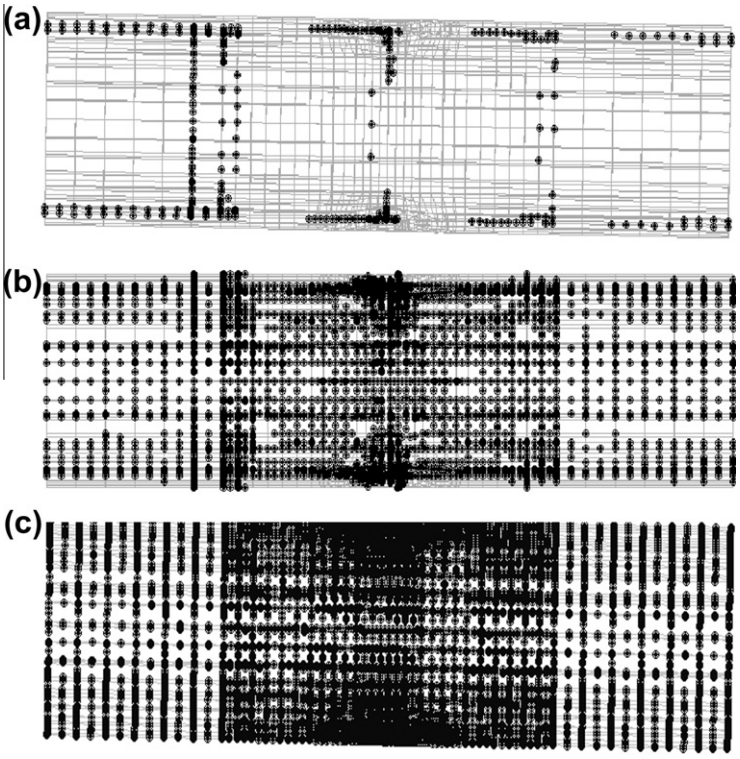


**Figure 30** Impact of tunnel depth to the plastic region in concrete lining. (a) Plastic region for RT (depth = 400 m), (b) plastic region for BT4 (depth = 600 m), (c) plastic region for BT5 (depth = 800 m).

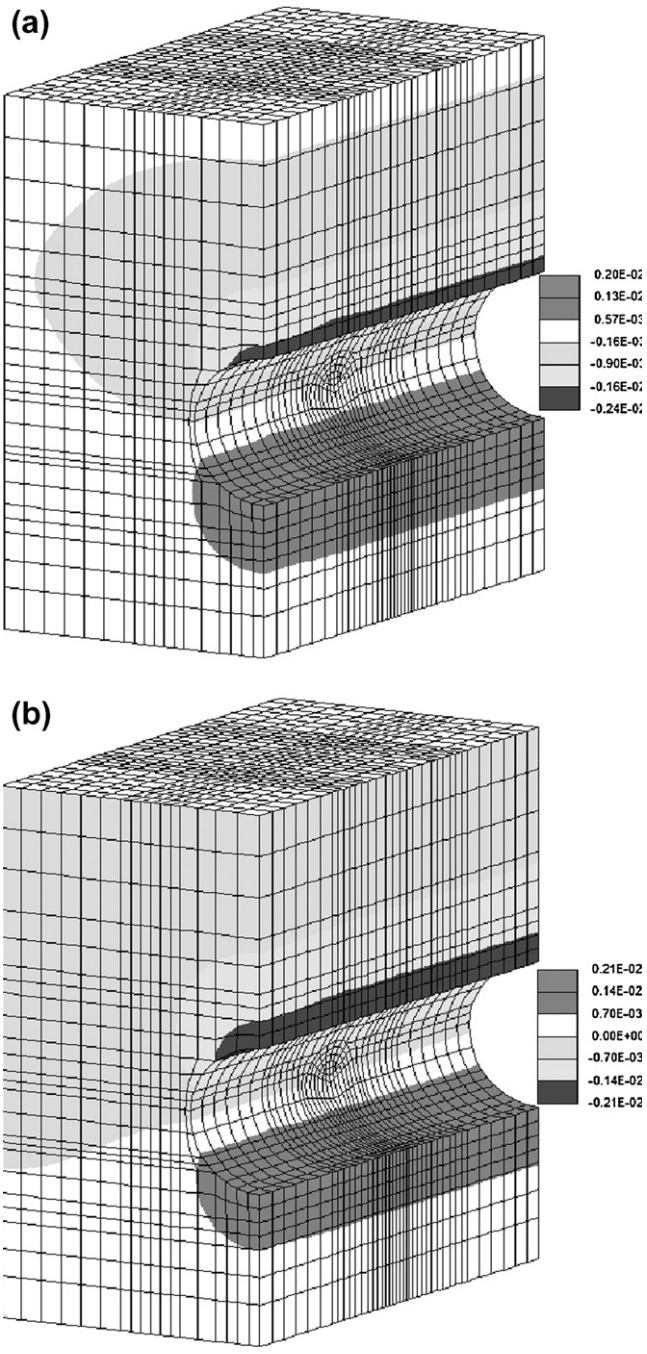


**Figure 31** *Z*-deformations for rock mass for different joint orientations. (a) $\alpha = 0.0$ (CT1), (b) $\alpha = 90.0$ (RT).

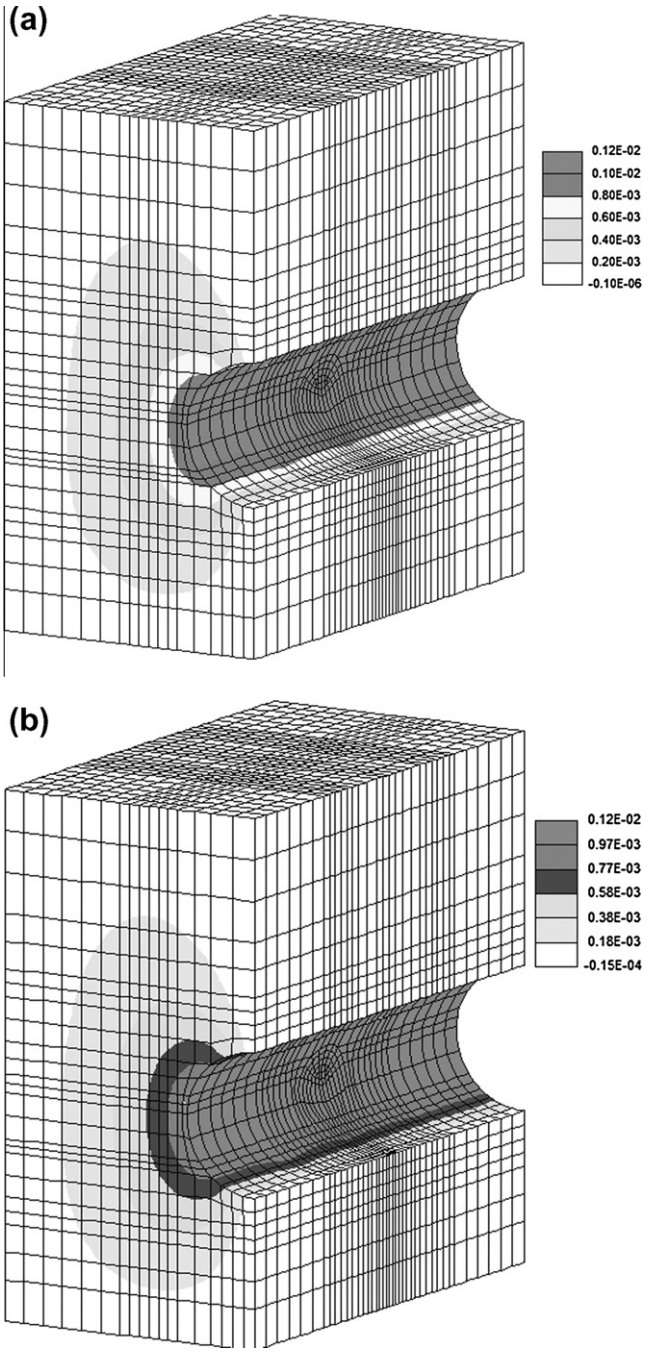


**Figure 32** *Y*-deformations for rock mass for different joint orientations. (a) $\alpha = 0.0$ (CT1), (b) $\alpha = 90.0$ (RT).

better confinement conditions of the surrounding rock and the arch action effect of the circular tunnel profile. In addition to the obtained smaller horizontal stresses ($\sigma_x$ and $\sigma_y$) induced on the side points coming from the surrounding rock mass, as displayed in Fig. 29b.

Therefore, the numerical results showed that higher stresses are obtained at higher depths causing local failures more than at shallower ones, as shown in Fig. 30a–c. The plastic formation begins to evolve nearly at 400 m depth (RT model). This could be realized from the significant evolution of the plastic regions with increasing the tunnel depth. These results agreed with the fact that, the higher stresses around the deeper tunnel cause rock mass to fail by toppling or sliding into the tunnel with great plastic evolution at higher depths, as shown in Fig. 30c.

## 12. With respect to joint orientation

### *12.1. Impact to rock mass*

The impact of different joint orientation ($\alpha$) on the rock mass is presented in Figs. 31–34. It appears that the joint

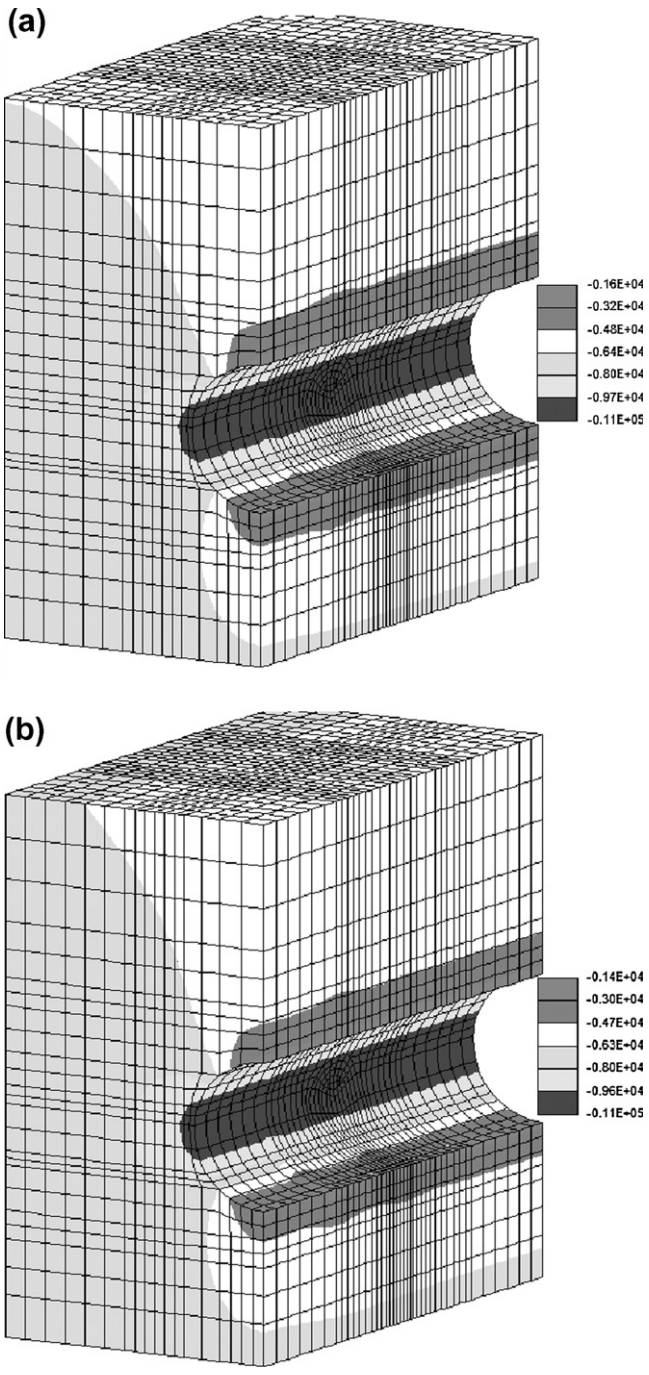


**Figure 33** $\sigma_Z$ for rock mass for different joint orientations. (a) $\alpha = 0.0$ (CT1), (b) $\alpha = 90.0$ (RT).

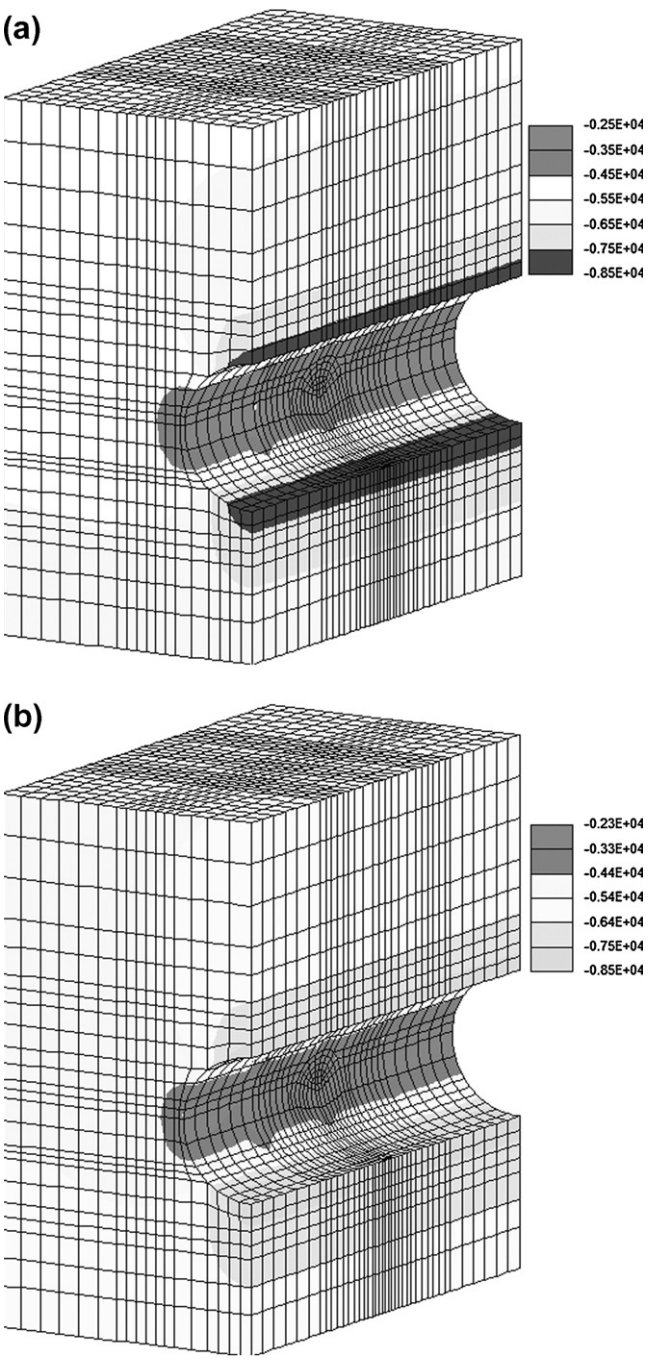


**Figure 34** $\sigma_Y$ for rock mass for different Joint orientations. (a) $\alpha = 0.0$ (CT1), (b) $\alpha = 90.0$ (RT).

orientation has a clear impact on both deformations (see Figs. 31 and 32) and stresses (see Figs. 33 and 34) for the surrounding rock mass. This effect comes from the influence of the joint orientation angle ($\alpha$) to the transformation matrix [$M$] presented in Eq. (8). Consequently, this joint orientation angle increases the evolution and the concentration of the effective stresses around the rock joints following the orientation of joints.

Also, there is a growth in the maximum deformations in horizontal direction normal to the joint direction ($\alpha = 90.0$) until reaching the side wall of the rock mass as shown in Fig. 31, and with expanding the compression zone to the roof of the rock mass (see Figs. 33 and 34).

### *12.2. Impact to concrete lining*

Figs. 35–38 show the weak impact of the joints orientation to the concrete lining. Nearly there is no influence of joints orientation for the obtained $Z$ deformation as shown in Fig. 35. For the $Y$ direction, with increasing the joint orientation angle, an increase in the deformation values is obtained with reducing the maximum deformation zones (see Fig. 36).

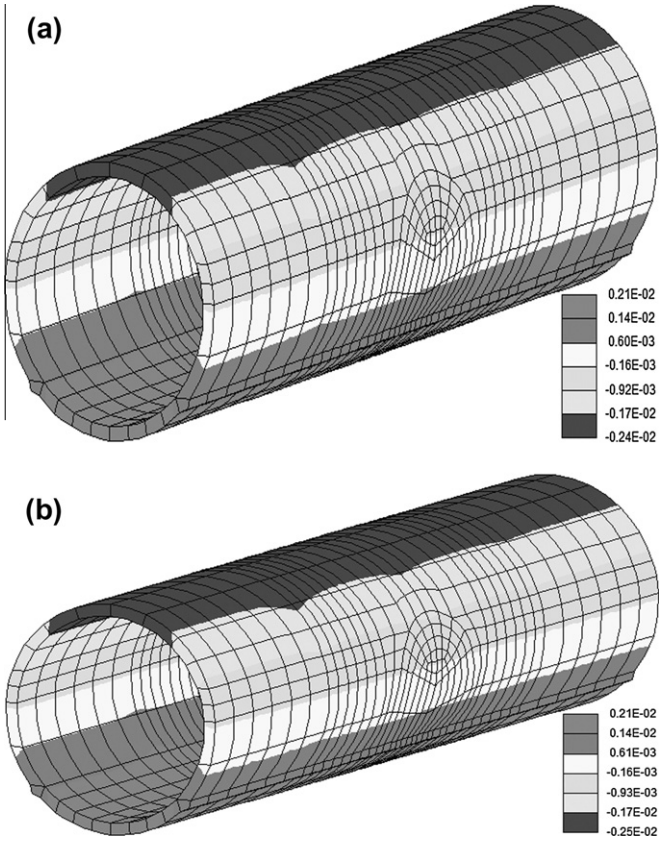


**Figure 35** *Z*-deformations for concrete lining for different joint orientations. (a) $\alpha = 0.0$ (CT1), (b) $\alpha = 90.0$ (RT).

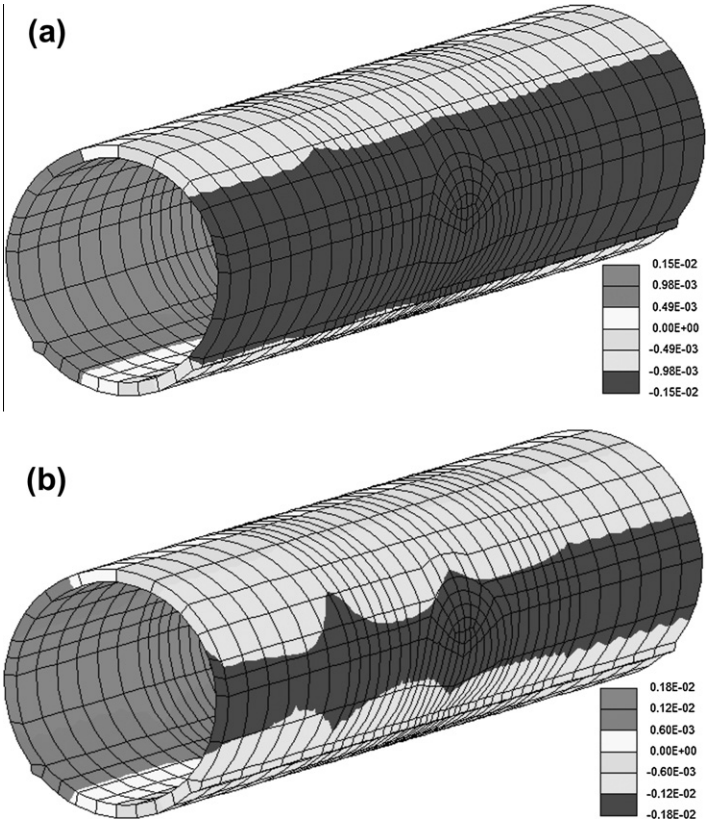


**Figure 36** *Y*-deformations for concrete lining for different joint orientations. (a) $\alpha = 0.0$ (CT1), (b) $\alpha = 90.0$ (RT).

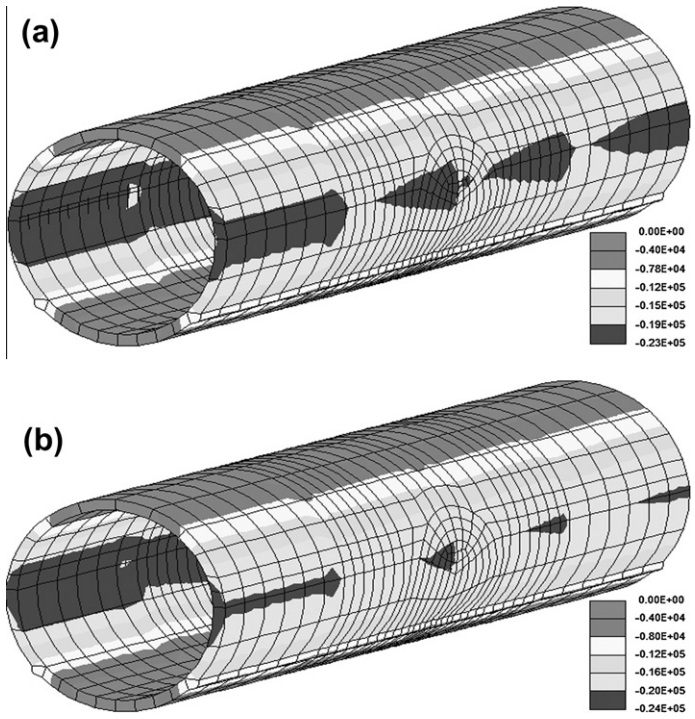


**Figure 37** $\sigma_Z$ for concrete lining for different joint orientations. (a) $\alpha = 0.0$ (CT1), (b) $\alpha = 90.0$ (RT).

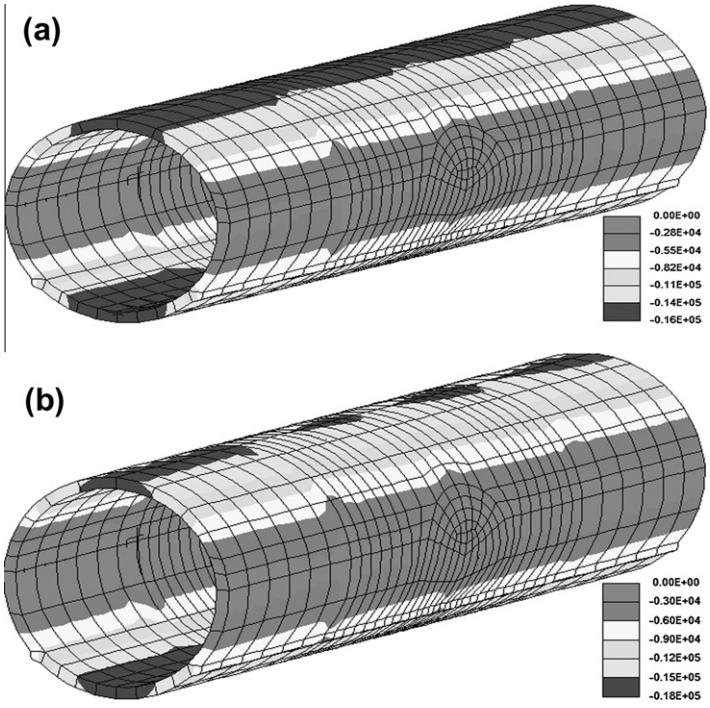


**Figure 38** $\sigma_Y$ for concrete lining for different joint orientations. (a) $\alpha = 0.0$ (CT1), (b) $\alpha = 90.0$ (RT).

The rock joint orientation has very slight impact to the induced stresses (see Figs. 37 and 38). With increasing the joint orientations, very small increase is generated for the induced stresses with reducing the maximum stresses zones. The increasing rate for the $Y$ direction is higher than that for the $Z$ direction with the same trend obtained in the corresponding deformations.

For cross-sectional results, this impact nearly disappears in relation to both the resulted deformations and stresses of the concrete lining, as shown in Fig. 39a and b. The joint

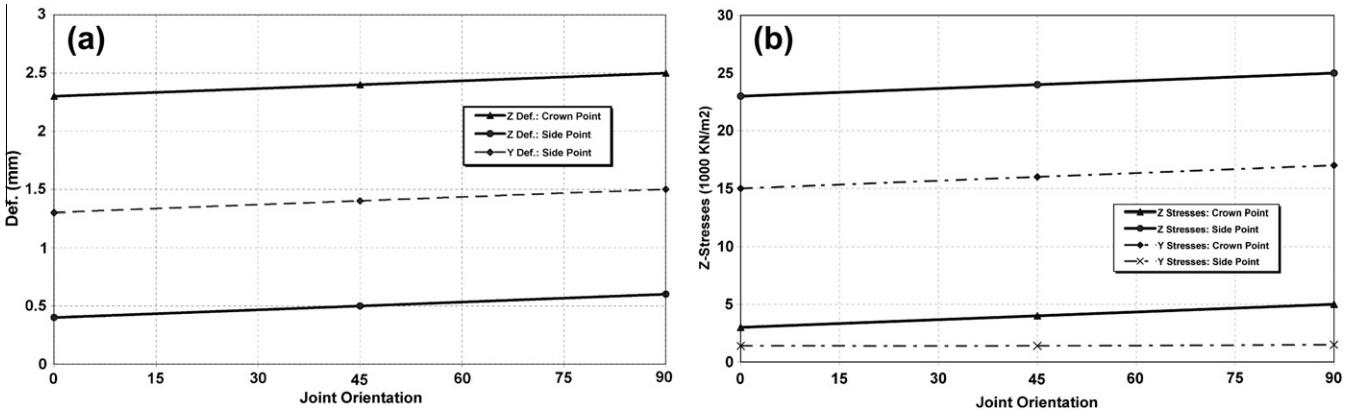


**Figure 39** Impact of joint orientation to the concrete lining. (a) Obtained deformations, (b) resulted stresses.

orientation nearly has no effect on the evolution of the plastic region. This may be due to the resulted higher compression stresses around the tunnel opening that may close the existing rock joints. In addition, the stable confinement condition around the tunnel tube because of the good quality of the used rock that decreases the transferred impact of changing the orientation to the concrete lining.

## 13. Conclusion

In this investigation, a parametric study was carried out in three-dimensional domain to study the effects of different joints configurations and tunnel depth on the behavior of a tunnel excavated in jointed rock mass. Various model cases were analyzed with different combinations of tunnel depth and joint configurations (density and orientation), respectively.

From the obtained numerical results, the following main conclusions are as follows:

- Deeper tunnels are subject to higher stresses which may lead to local failures that may not occur at shallower depths.
- Increasing the rock joint density reduces the loading carrying area with inducing stress concentration around the defects. Consequently, clear influence of the joint density is resulted for both the deformations and the induced stresses for the concrete lining and surrounding rock mass.
- Rock joint orientation has no significant impact on the concrete lining due to the good quality of the used rock mass and the closing of the rock joints by the induced compression stresses. But the impact of joint orientation is significant to the obtained deformation and induced stresses for surrounding rock mass.

## References

[1] Lee I-M, Park J-K. Stability analysis of tunnel key block: a case study. Tunn Undergr Space Technol 2000;16(4):452–92.
[2] Jaeger JC, Cook NGW. Fundamentals of rock mechanics. third ed. NY: Halsted Press; 1979.
[3] Jia P, Tang CA. Numerical study on failure mechanism of tunnel in jointed rock mass. Tunn Undergr Space Technol 2008:500–7.
[4] Sun J, Lu W, Zhu Q, Chen M. Elasto-plastic analysis of circular tunnels in jointed rock masses satisfy the Hoek–Brown failure criterion. J China Univ Mining Technol 2007;17(3):393–8.
[5] Yeung MR, Leong LL. Effects of joint attributes on tunnel stability. Int J Rock Mech Min Sci 1997;34(3–4):348.
[6] Hoek E, Brown ET. Practical estimates of rock mass strength. Int J Rock Mech Min Sci 1997;34(8):165–1186.
[7] Kwangho Y, Yeonjun P. A comparative modeling on the failure of shotcrete for the calculation of safety factors of tunnels. Tunn Undergr Space Technol 2006(21):433.
[8] Simo J, Ju JW. Strain and stress based continuum damage models – I. Formulation. Int J Solids Struct 1987;23:821–40.
[9] Madkour H, Saif Eldeen A. Computational elastoplastic crack modelling for RC beams. In: 2nd International conference on durability of concrete structures, ICDCS 2010, Hokkaido University, Sapporo, Japan, November; 2010. p. 643–52.
[10] Ottosen NS. A failure criterion for concrete, of engineering mechanics. Division 1977;105(EM4):527–35.
[11] CEB-FIP. Model Code 1990 Committee Euro-International du Beton. London: Thomas Telford; 1990.
[12] Madkour H. Numerical elastoplastic modelling of RC elements. Ain Shams J Civil Eng (ASJCE) 2010;1:53–69.
[13] Han DJ, Chen W. A non-uniform hardening plasticity model for concrete materials. Mech Mater 1985;4:283–302.
[14] Madkour H. Thermodynamic modeling of damage-plasticity for concrete and its application for tunneling. PhD dissertation, University of Innsbruck, Austria; 2004.
[15] Swoboda G, Shena XP, Rosas L. Damage model for jointed rock mass and its application to tunnelling. Comput Geotech 1998;22(3/4):183–203.
[16] ANSYS, Inc. ANSYS 11.0 user's documentation. Canonburg, PA, USA; 2007.
[17] Program system FINAL-finite element analyses program for linear and nonlinear structures, version 7.2; 2006.
[18] Guangyu S, Voyiadjis GZ. A new free energy for plastic damage analysis. Mech Res Commun 1997(24):377–83.

**H. Madkour** is a Assistant Professor in Civil Eng. Dept., Aswan Faculty of Engineering – South Valley University. PhD in 2000 from University of Innsbruck- Austria. He is author of many articles on; 3-D finite element modeling for progressive deteriorated concrete structures, Analysis of complex structures and fiber strengthened concrete elements, Elasto-plastic Modeling of R.C. structures, Experimental studying on retrofitting techniques for R.C. structures.